JOURNAL OF PETROLOGY

Journal of Petrology, 2015, Vol. 56, No. 7, 1309–1342
doi: 10.1093/petrology/egv037
Advance Access Publication Date: 13 August 2015
Original Article

OXFORD

Magma Transfer and Evolution in Channels within the Arc Crust: the Pyroxenitic Feeder Pipes of Sapat (Kohistan, Pakistan)

P. Bouilhol[1,2]*, M. W. Schmidt[2,3] and J.-P. Burg[2,3]

[1]Department of Earth Sciences, Durham University, Durham DH1 3LE, UK, [2]Department of Earth Sciences, ETH Zurich, 8092 Zurich, Switzerland and [3]University of Zurich, 8092 Zurich, Switzerland

*Corresponding author. Present address: Department of Earth Sciences, Durham University, Science Labs, Durham DH1 3LE, UK. Telephone: +44 (0) 191 33 42356. E-mail: pierre.bouilhol@durham.ac.uk

Received January 10, 2014; Accepted June 19, 2015

ABSTRACT

Our understanding of the mode of transfer and evolution of arc magmas in the lower arc crust is limited by the accessibility of arc roots, which are mainly documented by remote geophysical methods. At the same time, the fractionation processes of primitive parental melts defining a liquid line of descent from basalt to dacite are well defined by experimental petrology. However, the structural evidence for transfer of magmas evolving during their ascent remains basically uncharacterized. The Sapat Complex represents a lower crust segment of the exhumed Kohistan paleo-island arc and exposes kilometer-sized pyroxenite bodies that grew at the expense of host metagabbroic sill sequences. The largest of these pyroxenite bodies are mainly composed of wehrlite to olivine-clinopyroxenite, whereas the smaller bodies show a sequence of cumulative rocks, from ol-clinopyroxenite through various gabbros to tonalite. Inside the bodies, vertical magmatic and reactional structures indicate magma ascent accompanied by cumulate formation. Altogether, cumulates document the evolution of an initially primitive basaltic melt (at $\sim$7 kbar) that contained $\geq$5 wt % H_2O. After cotectic olivine and clinopyroxene fractionation, the appearance of hornblende at the expense of clinopyroxene marks a stepping stone in the melt evolution. From this point, the appearance of orthopyroxene and hornblende at the expense of olivine drives the magma towards an andesitic composition, from which the crystallization of An-rich plagioclase and hornblende drives the melt to evolve further. During peritectic hornblende crystallization fluid-precipitated assemblages occur showing that the melts have reached water-saturation while they were crystallizing and percolating, thus degassing H_2O-rich fluids. Structural observations, mineral and bulk-rock compositions, and calculated seismic P-wave velocities identify the ultramafic pipe-shaped bodies as magmatic conduits in which melt ascended from the mantle through the lower crust to feed upper crustal magma chambers and volcanic systems.

Key words: crystal fractionation; melt–rock reaction; arc–crust differentiation; magmatic conduit

INTRODUCTION

The processes involved in the formation and transfer of arc magmas are much less understood than the still debated magma generation and melt transfer processes at mid-oceanic ridges (e.g. Kelemen *et al.*, 1997; Nicolas *et al.*, 2008). Indeed, the migration mode from the source region in the mantle wedge towards the final emplacement site within the arc crust remains poorly defined. This is mainly because of the scarcity of exposed arc roots. The lower crustal section of the Kohistan paleo-island arc at Sapat was investigated to elucidate magma transfer, storage and evolution from the crust–mantle boundary towards upper crustal levels. We found ultramafic magmatic bodies that we interpret as subvertical magma channels and that may correspond to the deep structures geophysically

imaged at active subduction margins (e.g. Kodaira *et al.*, 2007).

Melting in the hot part of the mantle wedge, enhanced by slab-derived fluids and melts (Tatsumi *et al.*, 1983; Ulmer, 2001; Grove *et al.*, 2006), is a prerequisite to primary arc magma formation. Exposed mantle sections of paleo island arcs help in constraining the cumulate crystal proportions during early primitive arc magma differentiation at the crust–mantle boundary (DeBari & Coleman, 1989; DeBari & Sleep, 1991; Greene *et al.*, 2006; Garrido *et al.*, 2007; Bouilhol *et al.*, 2009). However, the wide range of suggested petrological processes leading to differentiated melts within the arc crust remains difficult to reconcile. Indeed, differentiation of hydrous basalts in the lower crust (Muntener *et al.*, 2001; Annen *et al.*, 2006; Ulmer, 2007; Jagoutz, 2010), dehydration melting of amphibolitized lower crust owing to basaltic underplating (Smith & Leeman, 1987; Petford & Gallagher, 2001; Jackson *et al.*, 2005) and fractional crystallization of basalts in shallow magma reservoirs (Sisson & Grove, 1993; Grove *et al.*, 1997; Martel *et al.*, 1999) would all ultimately lead to granitoid formation. In many crustal processes, amphibole plays a key role during the genesis of silica-rich magmas, either because amphibole hosts the water necessary to lower the solidus, or because its fractionation leads to SiO_2 enrichment in the evolving melt during crystallization (Cawthorn & O'Hara, 1976; Romick *et al.*, 1992; Grove *et al.*, 2003; Prouteau & Scaillet, 2003; Davidson *et al.*, 2007; Rodriguez *et al.*, 2007; Brophy, 2008). Equally important to the petrogenetic process is the morphology of the feeding system through which the parental melts rise, and in which an elusive amount of differentiation takes place. Despite 'hot zone' models (Annen *et al.*, 2006) being relevant to our understanding of the petrological record, natural examples of deep magmatic feeder pipes have been described only in a few Alaskan-type complexes (Murray, 1972).

In this study, we investigate the structures, petrography and chemistry of the rocks and minerals found in the mafic–ultramafic bodies of Sapat and show that these can be regarded as magmatic feeder pipes transferring magmas from the crust–mantle transition zone through the lower arc crust (~7 kbar) of Kohistan. Two pipes are investigated in detail, documenting (1) the cumulate assemblages that formed during the ascent of initially water-rich primitive magmas, (2) the corresponding magma evolution during reactive percolation of the evolving melt, and (3) the formation of a calc-alkaline suite leading to tonalitic rocks. The chemical evolution, together with the structures and modelled seismic P-wave velocities, suggest that the Sapat lower crust is an exposed example of the architecture of the deep roots of active island arc systems.

GEOLOGICAL SETTING

The Kohistan Complex (North Pakistan) represents an intra-oceanic island arc that formed during northward subduction of the Tethys Ocean in Mesozoic times (Tahirkheli, 1979; Burg, 2011) before being incorporated into the Himalayan orogen (Bouilhol *et al.*, 2013). It is now tectonically pinched between the Karakoram (active margin of Asia) and the Indian continents (Fig. 1). Kohistan is one of the rare places that offer the opportunity to explore an arc section close to the crust–mantle transition. There are three well-exposed lower crustal sections: (1) The Jijal section, which shows arc-mantle lithologies (Jan & Howie, 1981; Jan & Windley, 1990; Burg *et al.*, 1998; Dhuime *et al.*, 2007) intruded by garnet-gabbro (Bard, 1983; Burg *et al.*, 1998; Yamamoto & Yoshino, 1998; Ringuette *et al.*, 1999; Garrido *et al.*, 2006; Jagoutz, 2010) and overlain by a mid-Cretaceous sequence of calc-alkaline plutons, sills and dykes (Treloar *et al.*, 1996; Zeilinger, 2002); (2) the Chilas Complex ultramafic bodies, representing the apices of intra-arc mantle diapirs related to intra-arc extension at 85 Ma (Burg *et al.*, 1998, 2006; Schaltegger *et al.*, 2002; Jagoutz *et al.*, 2006; Burg, 2011); (3) the Sapat Complex (Fig. 1), formed between 105 and 99 Ma (Bouilhol *et al.*, 2011*b*), which includes ultramafic rocks (harzburgite, dunite and clinopyroxenite) overlain by interlayered fine-grained gabbros (~80%, varying from melano- to leucocratic), with minor hornblendites (~10%) and tonalitic/trondhjemitic (~10%) sills. The ultramafic rocks represent an exhumed piece of the frontal part of the arc mantle (Bouilhol *et al.*, 2009) and display evidence for percolation of mantle-derived primitive melts into harzburgite via porosity waves (Bouilhol *et al.*, 2011*a*). The fine-grained gabbro, hornblendite and tonalitic sills represent a lower crustal sequence (Fig. 1) generally affected by amphibolite- to greenschist-facies recrystallization during late Cretaceous exhumation of the area (Chamberlain *et al.*, 1991; Bouilhol *et al.*, 2012). This lower crustal sequence encloses kilometer-scale pyroxenite bodies, which are the subject of this study.

This study concentrates on two of the larger pyroxenite bodies. Less detailed field observations of seven other bodies have revealed the same rock types and relationships, thus allowing generalization of our results and extension of them to several other bodies that could only be spotted from a distance, confirmed from pebbles in rivers that drain them and more precisely located and mapped on satellite images (Fig. 1). The largest of the pyroxenite bodies (Pipe 1) is constituted of dunite, wehrlite and olivine (ol)-clinopyroxenite containing very minor plagioclase- and hornblende-bearing leucocratic patches. The second, smaller body (Pipe 2) exhibits a wider range of rock types ranging from ol-websterite to tonalite. Within each pipe different rock types may be intermingled on a meter scale, rendering the mapping of the internal parts of the pipes difficult and necessarily incomplete. Field photographs and schematic sections document the mesoscale relationships. Pipes 1 and 2 are linked by pegmatitic metagabbro (Fig. 1, and Bouilhol *et al.*, 2009, fig. 2).

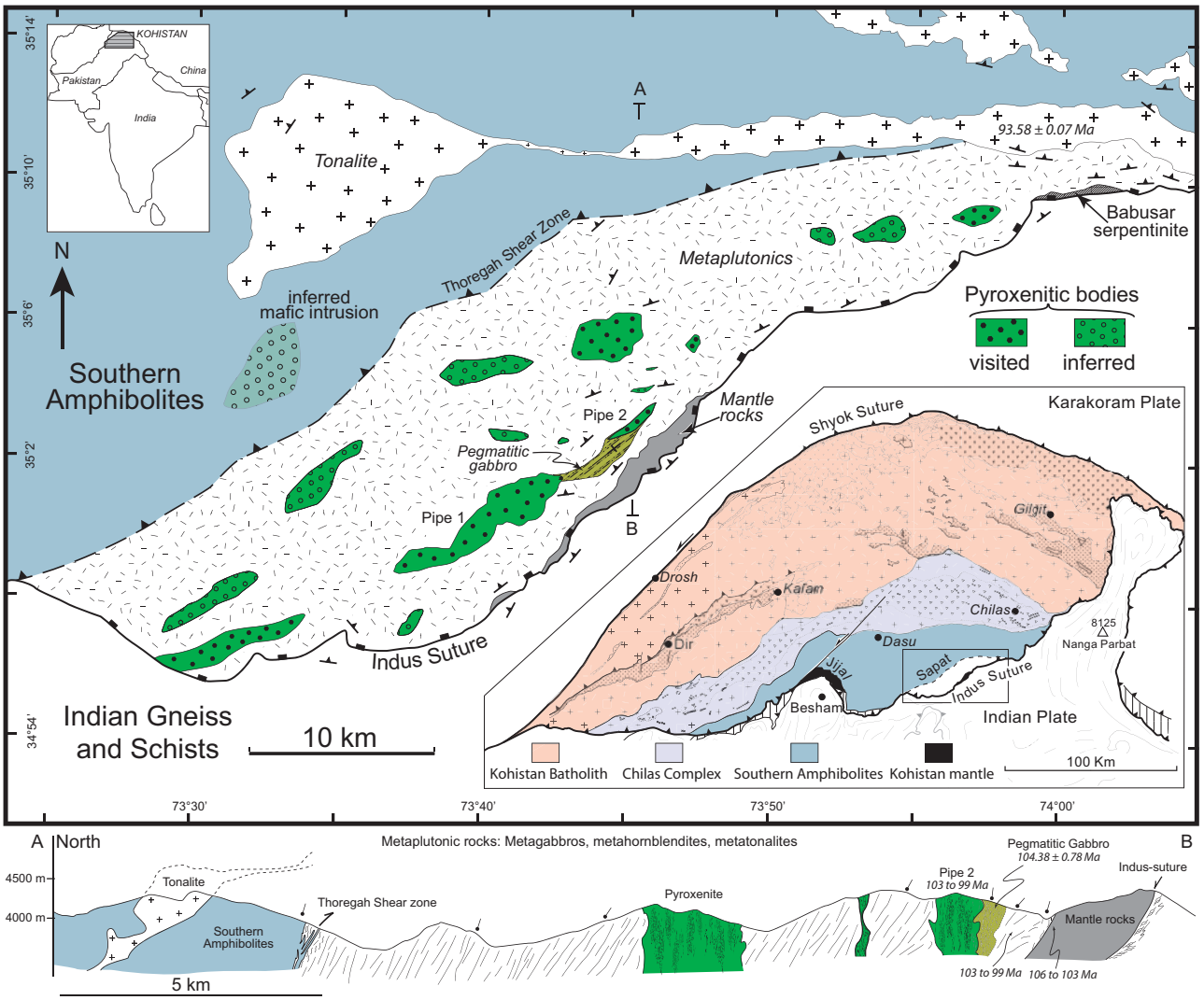

Fig. 1. Geological map of the Sapat Complex based on field mapping combined with SPOT + Landsat 7 ETM + images. The inferred pyroxenite bodies are based on landscape and satellite image observations. After Bouilhol *et al.* (2011*b*).

STRUCTURE OF THE PIPES

Contacts with host lower crust sills

Pipe 1 has an ellipsoidal shape of about 10 km × 2·5 km with the long axis striking N035, parallel to regional structural trends (Fig. 1). The fine-grained metagabbros surrounding Pipe 1 are generally equigranular within the vicinity (15–20 m) of the pipe (Fig. 2). However, in some places, a subvertical foliation subparallel to the sharp contact occurs in the ~5 m closest to the pyroxenite body (Fig. 2a). Very rare veins of fine-grained clinopyroxenite intrude the fine-grained metagabbros of the contact zone (Fig. 2a). The contact itself consists of a 50 cm wide, vertical zone in which fine-grained clinopyroxenite tends to invade and replace the fine-grained metagabbro (Fig. 2a and c). At the contact, some centimeter-sized pockets of gabbroic material represent remnants of the host-rock within the pyroxenite (Fig. 2a). To the east, Pipe 1 ends in a *c.* 50 m × 100 m zone of pyroxenite interfingered with pegmatitic metagabbro (Fig. 2e). The pyroxenite–pegmatitic metagabbro contact is sharp, subvertical and displays a strong, subvertical lineation marked by the ellipsoidal shape of clinopyroxene (cpx) aggregates that may be aligned into trails or form flames elongated along the foliation. These features, together with plastically undeformed crystals, characterize a magmatic foliation and lineation. Layers and alignments of cpx crystals within the pyroxenite are parallel to the foliation of the pegmatitic metagabbro.

Pipe 2 has an approximately 3·5 km long and 300 m wide ellipsoidal shape with its long axis trending N045 (Fig. 1). The contact with the fine-grained metagabbro is similar to that of Pipe 1 with an 80 cm wide, subvertical zone in which pyroxenite infiltrates the hosting metagabbro (Fig. 3). The north-dipping regional foliation and layering in the metagabbro disappears near the contact. The contact of pyroxenite–pegmatitic metagabbro is gradual over 1–2 m, with the plagioclase proportion increasing towards the pegmatitic metagabbro. The magmatic foliation in the pegmatitic metagabbro is, like

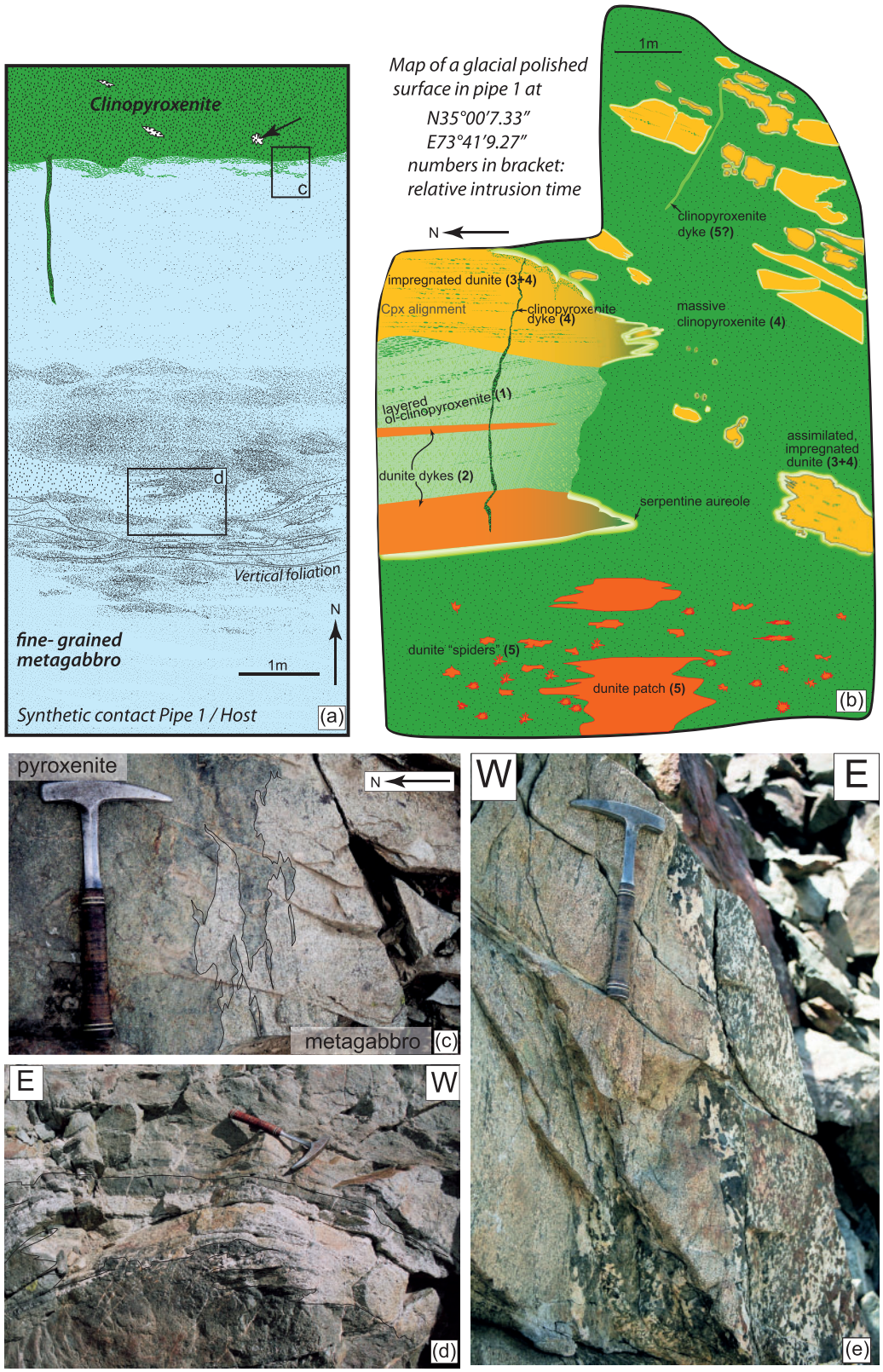

Fig. 2. Aspects of Pipe 1 internal relationships and contact with the surrounding low-grade, interlayered gabbros. (a) Sketch map view of the contact between Pipe 1 and the host fine-grained metagabbros. Lettered frames refer to the field photographs (c) and (d). (b) Small-scale sketch map of a typical internal relationship between dunites and clinopyroxenites in Pipe 1. These relationships indicate interaction between percolating melt and crystallization products. (c) Photograph of the southern, subvertical contact of pipe pyroxenite invading the host, fine-grained metagabbro (35°00·324′N, 73°41·877′E). (d) Lower-crustal host-rocks ~5 m from the contact with Pipe 1, showing intermingled melano- and leuco-gabbroic facies with a subvertical magmatic foliation. (e) Eastern tip of Pipe 1 where fine-grained and pegmatitic metagabbros display a vertical magmatic foliation and lineation (35°01·529′N, 73°42·648′E).

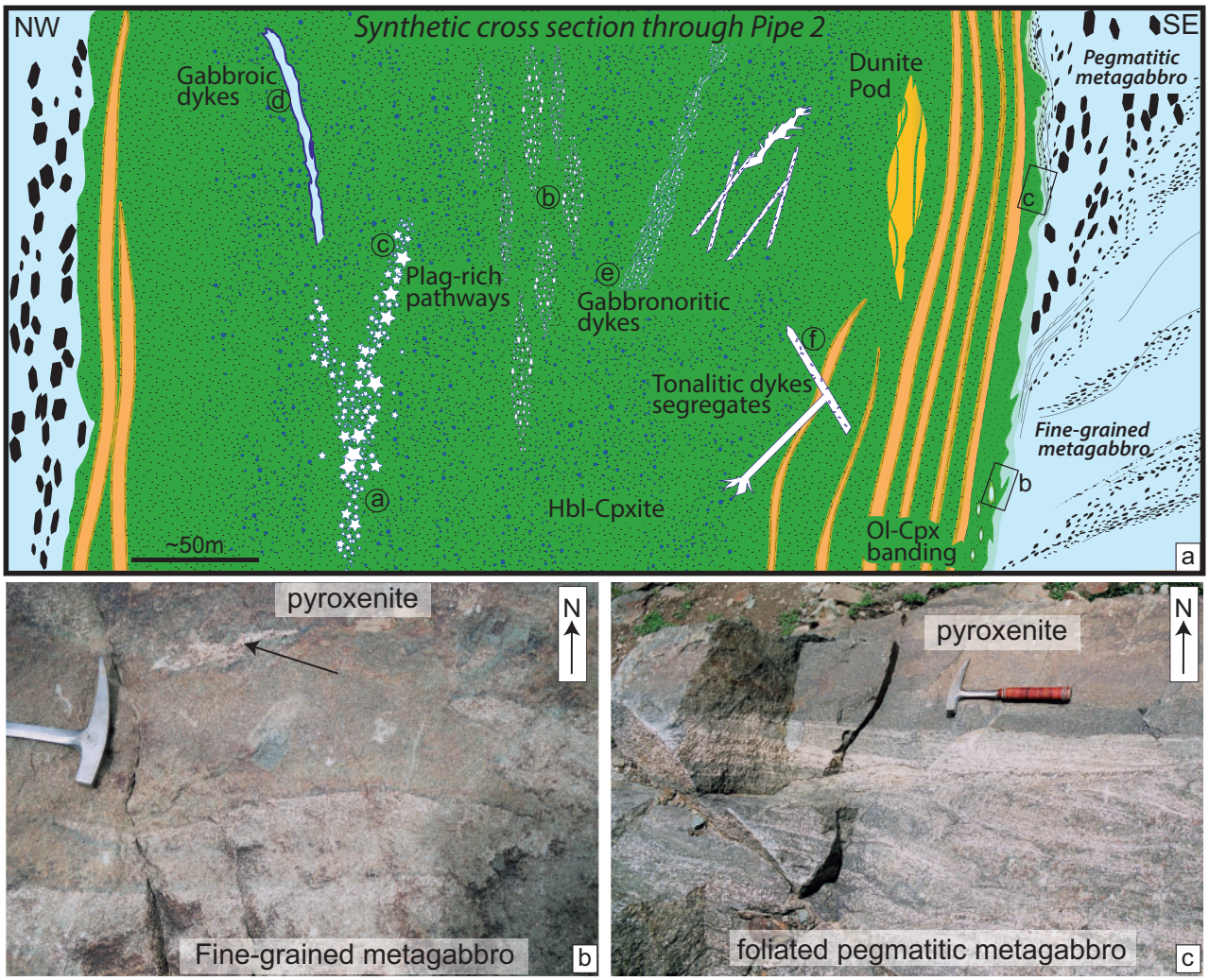

Fig. 3. Boundaries and rock associations in Pipe 2. (a) Schematic cross-section through Pipe 2. Lettered rectangles refer to field photographs (c) and (d); circled letters refer to field photographs in Fig. 5. (b) Contact between host fine-grained metagabbro and pipe pyroxenite. Arrow indicates an enclave of assimilated metagabbro (35°03·569′N, 73°45·850′E). (c) Magmatic vertical fabric in pegmatitic metagabbro with reduced grain size at the contact with the pipe pyroxenite (35°03·765′N, 73°45·862′E).

the contact, subvertical (Fig. 3). The tips of Pipe 2 are not exposed or could not be reached because of the very steep relief.

Olivine-clinopyroxenite body (Pipe 1)

The volumetrically most important lithologies of Pipe 1 are wehrlite and clinopyroxenite with millimeter- to centimeter-sized grains (Fig. 4). The relationships between the various rock types are summarized in Fig. 2b. Wehrlites and clinopyroxenites show a wide range of textures, from equant, fine-grained to pegmatitic, to inequigranular, with subhedral to anhedral cpx. Crystallization of olivine (ol) before cpx (documented by subhedral cpx in an ol matrix), of cpx before ol (anhedral cpx with subhedral ol) and co-crystallization of both (equant texture) are equally abundant within the body. Local layering marked by different modal proportions of ol and cpx, magmatic slumps and cross bedding attest to melt dynamics. Subvertical, centimeter- to decimeter-wide dykes of fine-grained ol-clinopyroxenite intrude the ol-clinopyroxenite groundmass with sharp boundaries, whereas subvertical dykes of pegmatitic ol-clinopyroxenite with meter-long cpx have diffuse boundaries with the host-rock (Figs 2b and 4). Within the clinopyroxenites, geodes with radially grown cpx are common and have diameters of up to several decimeters (Fig. 4a). Dunites occur as *c.* 100 m^2 bodies within the pyroxenites or as dykes and patches. Rare pegmatitic, hornblende-bearing leucocratic patches (10–100 cm wide and 0·5–20 m long) exhibit a hornblende rim at the border with the surrounding pyroxenite (Fig. 4b). Shallowly north-dipping, decimeter-wide hbl-bearing tonalite dykes cut the pyroxenite structures and become more abundant up-section (see also Bouilhol *et al.*, 2011*b*, fig. 2). These tonalitic to trondhjemitic dykes are found only within the pipe.

Equigranular ol-clinopyroxenite often exhibits a 'spider' texture consisting of star-shaped centimeter- to decimeter-sized ol aggregates (Fig. 2b). In three dimensions, these aggregates represent subvertical tubules

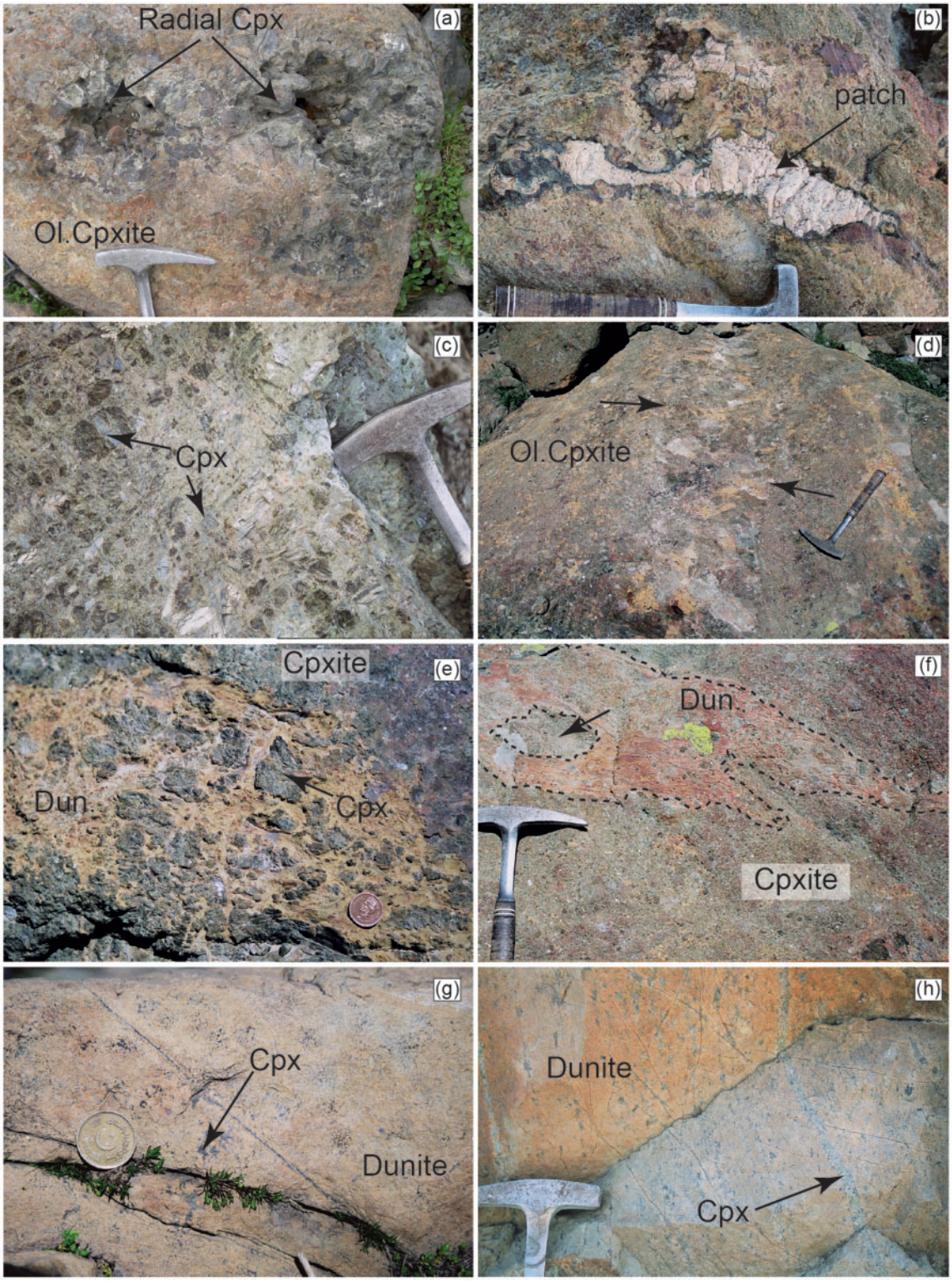

Fig. 4. Rock associations in Pipe 1; abbreviations as in the text. (a) Geodes in pyroxenite showing radial growth of cpx from the wall inwards. (b) Leucocratic patch with amphibole rim (35°00·339′N, 73°41·805′E) representing the most evolved rock found in Pipe 1. (c) Magmatic inequigranular texture in hbl-bearing clinopyroxenite (sample P7; 35°01·010′N, 73°42·166′E) in which >1 cm-sized cpx grains occur in a matrix of fine cpx + hbl. (d) Vertical pegmatitic clinopyroxenite dyke with antitaxial coarse cpx. The diffuse contact with the host ol-clinopyroxenite should be noted (arrows) (35°00·666′N, 73°42·088′E). (e) Reacted and corroded cpx in a vertical tubular dunite vein (dun) (35°00·666′N, 73°42·088′E). (f) Diffuse dunite dyke showing assimilated clinopyroxenite pieces (arrow) (35°00·666′N, 73°42·088′E). (g) Cpx at ol grain boundaries (arrow) in massive dunite (light-coloured background) indicating melt percolation (35°00·936′N, 73°42·252′E). (h) Vertically aligned cpx forming trails (arrow) in dunite (35°00·733′N, 73°41·927′E).

invading the host ol-clinopyroxenite. These tubules tend to coalesce, surround, isolate, and corrode the host clinopyroxenite (Fig. 4e). This type of texture occurs near diffuse, subvertical dunite intrusions and patches that corrode and assimilate cpx crystals and aggregates of the host ol-clinopyroxenite groundmass (Fig. 4f). Isolated cpx crystals often show corroded boundaries (Fig. 4e) and cpx aggregates in dunite have light-colored serpentine rims. Dunite intrusions contain thin flames of serpentine organized into a network parallel to the dyke walls. Massive dunites have diffuse and gradual boundaries with the ol-clinopyroxenite. Within these dunite masses, cpx may be organized in cockades at grain boundaries of ol (Fig. 4g), or may be aligned into trails (Fig. 4h). Cpx in dunite may also form flames or may occur in veins and dykes with diffuse boundaries. Some dunites contain euhedral, millimeter-sized spinels (spl) and relict corroded cpx up to 10 cm.

Amphibole–plagioclase olivine-websterite body (Pipe 2)

Pipe 2 is dominated by massive ol-websterite and ol-clinopyroxenite (Fig. 3) in which amphibole is ubiquitous. Varying modal proportions of cpx and ol define a near-vertical banding. Elongated dunite bodies of *c.* 10 m^2 are intruded by ol-clinopyroxenite with diffuse boundaries, the cpx content in the dunite increasing towards the ol-clinopyroxenite. Within the pipe, and mainly in its core, subvertical, tubular zones of plag–hbl-bearing ol-websterite (Figs 3a and 5a) have ellipsoidal shapes in horizontal section with long axes perpendicular to the long axis of the body (Fig. 5b). Hbl and plag formed at grain boundaries within these zones (Fig. 5a). In some places, plagioclase has totally overprinted the host pyroxenite (Fig. 5c). Volumetrically minor hbl-gabbro (Fig. 5d), and hbl-gabbronorites (Fig. 5e) form subvertical, 0·1–1 m thick dykes whose borders may be diffuse (Fig. 5e) or sharp, but marked by a ubiquitous hbl rim (Fig. 5d). North-dipping, centimeter to decimeter thick tonalite dykes, striking generally parallel to the pipe boundaries and locally forming conjugate sets, cut across all structures (Fig. 5f) within the pipe. These tonalites show a wide range of textures and modal compositions. Amphibole crystals are usually euhedral, rooted on the dyke walls, and may reach tens of centimeters in length. Fine amphibole grains border the dykes, isolating the tonalite from the host pyroxenite, and are most probably a reaction product between the tonalite melt and the host rock. Millimeter- to multi-centimeter-sized garnets are found within these tonalitic dykes. Rare gabbroic dykes cut across all structures.

Dunitic bodies

Several dunite bodies, hundreds of meters in diameter, were recognized in the field. They display structural aspects similar to those of the pyroxenite pipes. Much smaller than the pyroxene-dominated bodies, they are more difficult to spot in the field. Three of them have been pinpointed; one of them has been surveyed. The studied body is composed of massive dunite with serpentine at olivine grain boundaries. No contact with the surrounding fine-grained metagabbros was exposed, but from the map shape of this body in an area of strong relief, we deduce that this body is subvertical. As we did not investigate these mascoscopically homogeneous dunites geochemically, they will not be discussed further.

PETROGRAPHY

Pipe 1

Clinopyroxenites show a typical adcumulate texture with xenomorphic, strongly lobate and imbricated cpx (Fig. 6a). Intercumulus and grain boundary phases comprise amphibole, spinel, chlorite, and serpentine.

Magmatic textures

Adcumulus cpx crystals typically range from a few millimeters to centimeters in size, but meter long cpx exist. Cpx locally has a grayish color and a clear cleavage often related to amphibole lamellae and magnetite trails (Fig. 6b). In most cases, this adcumulus cpx (cpx_1) forms a comb texture with smaller cpx (cpx_2). The comb texture is systematically associated with amphibole, either at the contact between cpx_1 and cpx_2, or as patches and exsolution lamellae in cpx_1 (Fig. 6c). Cpx_1 often shows rims recrystallized to cpx_2. Fine grains of cpx_2 may also be present at grain boundaries of cpx_1 (Fig. 6b). Millimeter-sized cpx_2 invade ol grain boundaries in dunites. Subhedral to anhedral spl are common inclusions in cpx.

Fresh, coarse dunite shows a heterogeneous grain size with strongly undulose, millimeter-sized, tabular ol grains and euhedral chromite grains within a matrix of finer ol grains that show 120° triple junctions (Fig. 6e). A few micrometer-sized corroded cpx grains are present in some places together with a brownish mineral phase too small to be identified (labelled Res. in Fig. 6f).

Fluid-related textures

Magmatic ol in the ol-clinopyroxenite is mostly recrystallized to mesh-serpentine and often associated with calcite and magnetite within a network with a strong preferred orientation. A second generation of ol replaces serpentine in net-like features or as large grains with inclusions of magnetite and/or calcite (Fig. 6d). Geodes in the clinopyroxenites are filled with a cpx + epidote + chlorite + titanite assemblage. The matrix of the leucocratic patches consists of epidote aggregates, with millimeter-sized amphibole, chlorite and minor nests of tens of micrometers long cpx. Amphiboles show recrystallization rims, and millimeter-sized euhedral amphibole overgrows chlorite. These leucocratic patches have little of their magmatic mineralogy left.

Fig. 5. Lithologies in Pipe 2. (a) Impregnation feature on a vertical wall with plag and hbl at grain boundaries in the host Hbl-pyroxenite (35°03·000′N, 73°45·307′E). (b) Same features as in (a) but on a horizontal plane view showing the lens-shaped vertical and parallel plag–hbl rich zones (35°03·341′N, 73°45·565′E). (c) Highly reacted pyroxenite with remnants of pyroxenite in a plag-rich domain (white) (35°03·317′N, 73°45·273′E). (d) Vertical dyke of hbl-gabbro with reactional hbl rim (black arrow) in pyroxenite with hbl (white arrow) at grain boundaries (35°04·086′N, 73°45·780′E). (e) Vertical dyke of hbl-gabbronorite with diffuse contact (arrow) [next to dyke in (d)]. (f) Subvertical tonalitic dyke with reactional hbl rim (arrow) and epitaxial hbl cross-cutting alternating cpx–ol-rich bands (35°04·022′N, 73°45·059′E).

Pipe 2

Magmatic textures

The ol-clinopyroxenites of this body often show an adcumulus texture. The transition between ol- and cpx-rich horizons is defined by a heteradcumulus texture (Figs 3 and 7a). A few opx grains with an adcumulus texture are observed in the ol-clinopyroxenite. Amphibole replaces cpx (Fig. 7b) extensively, and is also present at grain boundaries or builds a heteradcumulus texture with ol and cpx. Calcite and/or Cr-clinochlore are locally associated with amphibole. Amphibole, calcite and Cr-clinochlore and Cr-spl are occasional inclusions in ol. Micrometer-sized garnet, green spinel (spl) and amphibole usually make the groundmass of the pyroxenites.

Within dunite pods, ol is present as adcumulus crystals. Magnetite, titanomagnetite and FeNi sulfides are present as inclusions and at grain boundaries.

Next to the plag–hbl-bearing ol-websterite zones the replacement of cpx by amphibole becomes more pervasive and is associated with green spl and opx (Fig. 7c). Opx is also found at grain boundaries and often overgrows ol (Fig. 7d), which indicates a peritectic origin. Rarely, interstitial amphibole hosts cpx + green spl symplectites.

Within plag–hbl-bearing ol-websterite zones, plag systematically invades grain boundaries and often includes amphibole. Olivine and plag are never in direct contact but show various mineral associations in reaction rims. These may be constituted by opx or

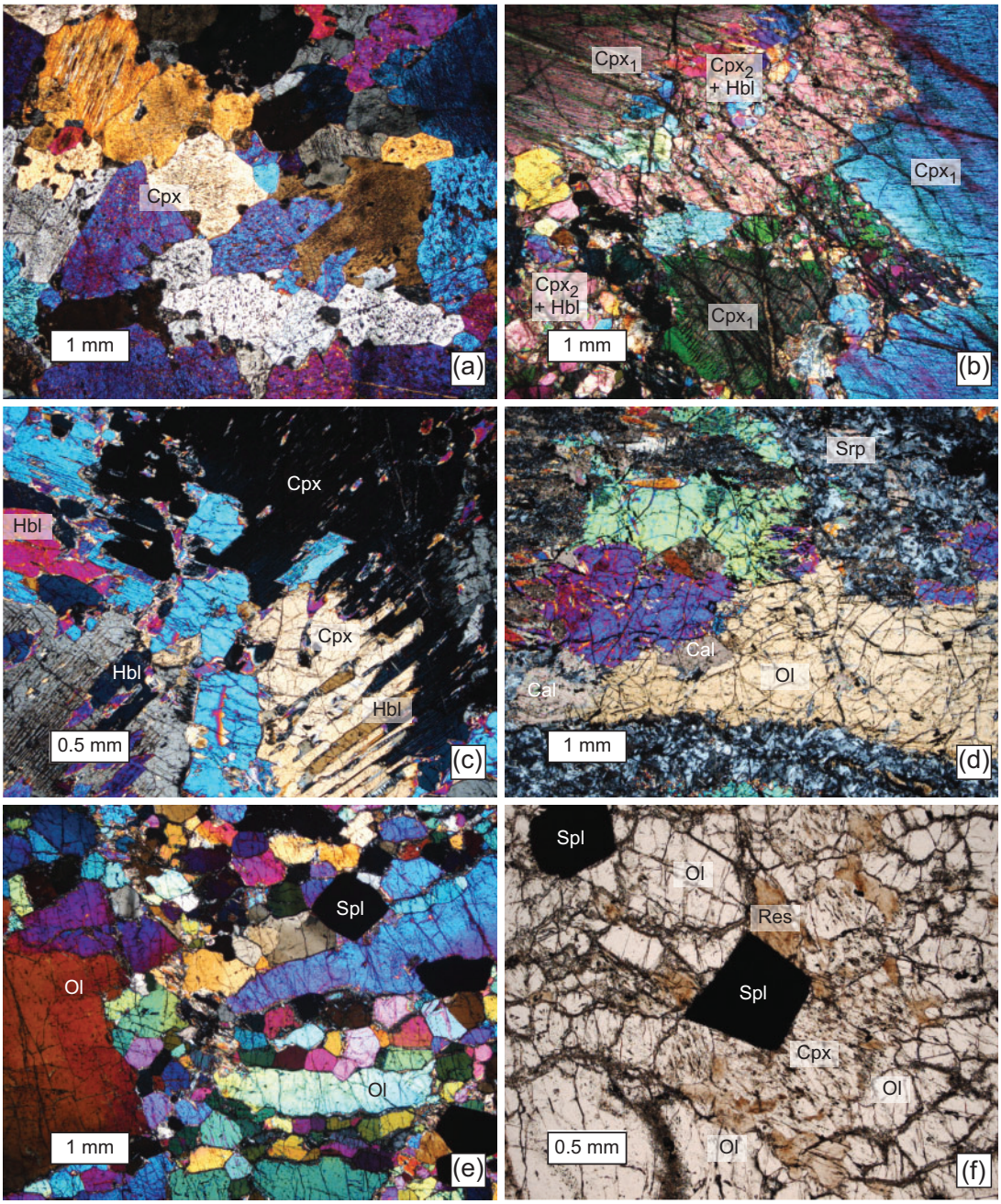

Fig. 6. Photomicrographs in cross-polarized light (a–e) and plane-polarized light (f) illustrating magmatic and sub-solidus features in Pipe 1. Abbreviations as in the text. (a) Typical adcumulate texture in clinopyroxenite. (b) Two generations of cpx in a hbl-pyroxenite (sample P7). Large cpx_1 with tremolite marking the cpx cleavage and cpx_2 + hbl forming the matrix. (c) Hbl and cpx intergrown in a comb texture in hbl-clinopyroxenite P13. (d) Second ol generation overgrowing serpentine and including calcite in a serpentinized dunite. (e) Typical porphyroclastic texture in dunite with euhedral chrome spl (sample P22). (f) Secondary dunite, showing relict cpx after ol–sp formation. Res, residual after cpx breakdown.

amphibole only, but are more commonly symplectites of amphibole + green spl ± opx (Fig. 7e). Symplectite growth may begin at ol surfaces but is also observed on amphibole coating ol (Fig. 7e and f). Cpx is almost absent from these rocks, the mineralogy of which comprises plag + hbl + opx + green spl + relict ol enclosed in symplectites.

Hbl-gabbros contain subhedral amphibole grains in a matrix of anhedral plag. Dyke borders show co-crystallization of plag and antitaxial amphibole needles on the dyke side, whereas the host side is fully replaced by subhedral amphibole and ilmenite (Fig. 5d). These subhedral amphibole grains gradually become interstitial in the pyroxenite host, suggesting that they originate from a reaction between the hbl-gabbro melt and the host pyroxenite.

Hbl-gabbronorite dykes contain anhedral opx, cpx and amphibole in a matrix of xenomorphic plag (Fig. 7g). Granophyric textures with opx + cpx + amphibole intergrowth are present.

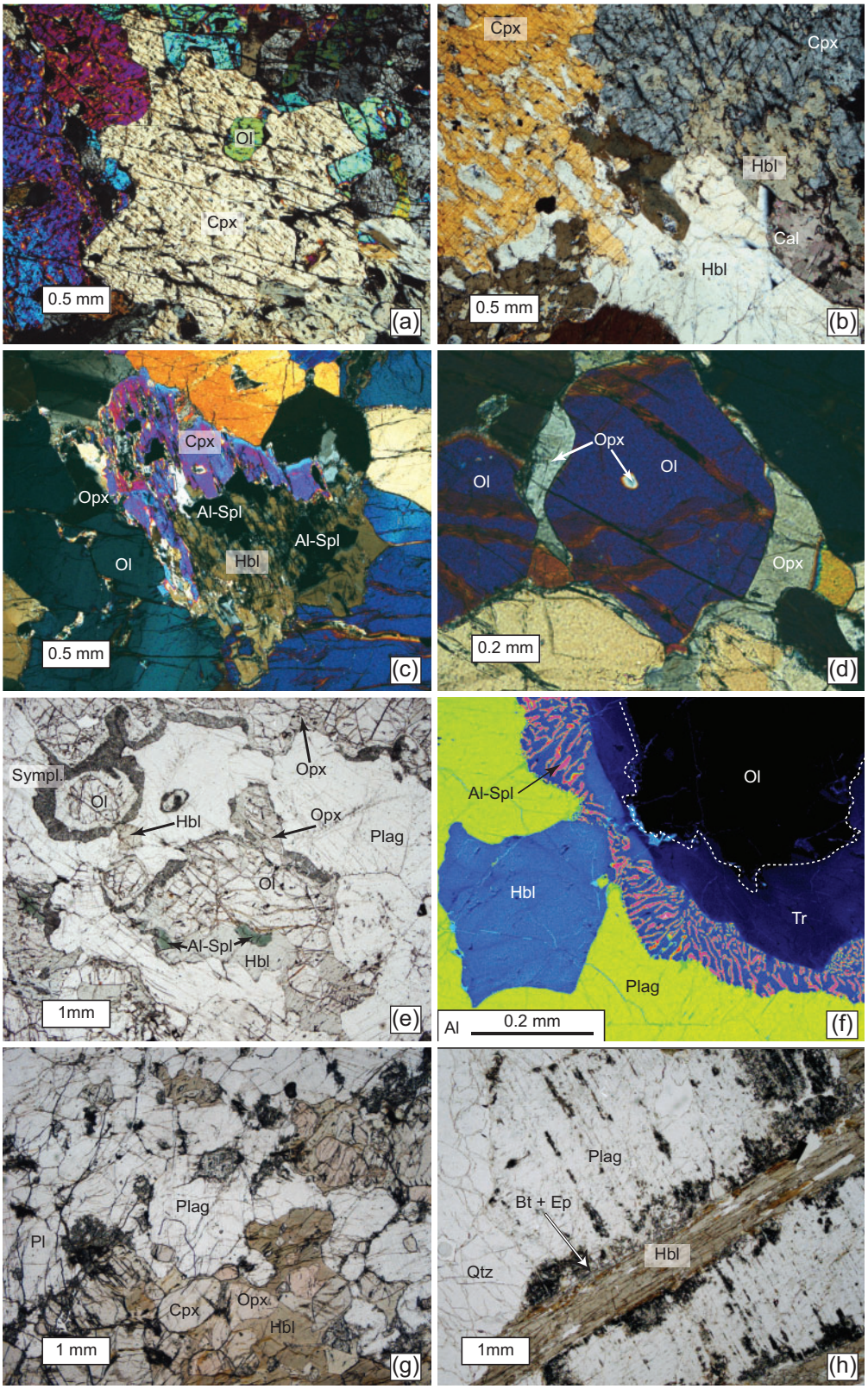

Fig. 7. Petrographic observations in cross-polarized light (a–d) and plane-polarized light (e, g, h) of the main rock types of Pipe 2. (a) Heteradcumulate texture at the interface between cpx- and ol-rich bands (sample P42). (b) Hbl replacing cpx texture (sample P47; note the presence of calcite). (c) Cpx being replaced by hbl + deep green spl (note opx at grain boundaries; sample P62). (d) Opx growing at grain boundaries and replacing ol, denoting peritectic reaction (sample P62). (e) Fully reacted pyroxenite with plag at grain boundaries and opx or hbl or opx + hbl + green spl coating ol. Green spl + hbl symplectites are also present coating either ol or opx or hbl (sample P52). (f) Al Kα map of a symplectite coating hbl-rimmed ol. Magmatic hbl coats ol before plag crystallization, then the symplectite forms as the ol reacts with plag in HT sub-solidus conditions in the presence of a fluid phase. The symplectite rooted in tremolite shows that the tremolite grew at the expanse of ol via diffusion under greenschist-facies conditions. (g) Magmatic texture in hbl-gabbronorite. (h) Hbl lath rimmed by magmatic epidote and minute biotite in a tonalite dyke (sample P63).

Hbl-tonalites contain euhedral to subhedral amphibole with plag and quartz as matrix phases (Fig. 7h). Plagioclase and quartz are graphically intergrown, indicating eutectic crystallization. Large high-birefringence epidote grains, crystallized before quartz and feldspar, are of magmatic origin (Zen & Hammarstrom, 1984) and occur together with plag. A few microscopic biotite grains are found in contact with amphibole. Titanium oxides and ilmenite are inclusions in amphibole and plag. Zircon and apatite are common minor phases.

Within hbl-gabbro dykes, millimeter-sized euhedral garnets are found in plag. Within tonalitic dykes, garnet is associated with green amphibole and ilmenite in plag.

Fluid-assisted crystallization

Cpx and amphibole are replaced by secondary tremolite whereas chlorite is omnipresent at grain boundaries. Plagioclase grain boundaries and fractures are often coated with secondary bluish-green amphibole and epidote, locally together with corundum or garnet. The bluish-green amphibole may also rim magmatic amphibole, in particular at the interface between the latter and plag. Cu and Zn sulfides are frequent in this paragenesis.

Interpretation of structures and textures

Within Pipe 1 single magma pathways are represented by dunite and ol-clinopyroxenite that cut, infiltrate and react with pyroxenites and vice versa (Fig. 2b). The general attitude of all structures, in particular the within-pipe tubules and dykes, is subvertical. As magmatic foliation and lineation are aligned with the direction of melt movement, we infer that melt circulation was also subvertical (in the present-day attitude). The pipe-filling rocks have been formed by processes including a combination of crystallization, melt evolution and peritectic reaction with previous cumulates, all related to the rising melt. We envision the following: a primitive, Cpx-undersaturated melt crystallizes ol first, generating dunite; then cpx crystallizes together with ol on a cotectic generating ol-clinopyroxenite. Small variations in melt composition, pressure, temperature, or the nature and amount of assimilated material move the liquid composition off the ol–cpx cotectic, leading to saturation in ol or cpx only. Percolation of cooling melts would further lead to crystallization of peritectic cpx (in most cases cpx_2) and amphibole, thus generating hbl-bearing clinopyroxenites. A new batch of ol-saturated melt percolating through cpx-rich lithologies dissolves cpx and crystallizes ol to generate dunitic patches, 'pathways' and 'spider textures' with relict, corroded cpx. Percolation of a cpx-saturated melt into dunite may result in a modal ol-clinopyroxenite. Combinations of crystallization and percolation led to the variety of observed textures and relationships between ol, different generations of cpx and amphibole (Fig. 2b). A trapped fraction of residual melt may have crystallized the leucocratic patches, which would correspond to the end of the crystallization–reaction process.

Within Pipe 2 magmatic structures are also subvertical. There are only a few dunite pods, impregnated by cpx, suggesting that most of the melt of Pipe 2 was ol + cpx ± opx saturated, consistent with the volumetrically dominant ol-websterite and ol-clinopyroxenite. Amphibole replacing cpx suggests a peritectic reaction between cpx and a hydrous melt, as for the amphiboles in Pipe 1. The appearance of opx at the expense of ol suggests peritectic reaction between melt and ol. The crystallization of opx, plag and hbl at grain boundaries within subvertical channels is attributed to magma percolation that led to the disappearance of cpx in fully reacted pyroxenites. The fully reacted pyroxenites indicate disequilibrium between the host pyroxenite and the percolating melt (Fig. 5c). Within the most differentiated dykes, mineral phases (cpx, opx, amph, plag ± ep + qtz) become cumulus phases following the classical calc-alkaline crystallization sequence. These dykes also show reaction relationships with the host hbl-pyroxenite, suggesting a more evolved melt for the latter. Hbl crystallized early within the hbl-gabbro and tonalite, as shown by its euhedral habit.

Two types of fluid-associated texture can be distinguished. The first type is related to near-solidus recrystallization during magma flow in the pipes. The corresponding features are (1) geodes filled with hydrous phases, (2) cpx_1 containing amphibole or serpentine and chlorite absent in cpx_2, (3) the ubiquitous presence of calcite associated with peritectic amphibole and serpentine, and enclosed in serpentine back-reacted to olivine, (4) bluish-green amphibole associated with epidote, chlorite and sulfides in Pipe 2 and (5) serpentine-rimmed fragments of assimilated material. The second type corresponds to late recrystallization affecting all phases, most probably owing to a greenschist-facies overprint (chlorite + tremolite + epidote) during exhumation.

In summary, the pyroxenite bodies represent magmatic conduits through which melts migrated, in part crystallizing but also reacting with the cumulate products of previously rising melts.

MINERAL AND BULK-ROCK COMPOSITIONS

The bulk-rock compositions mainly reflect the mineral modes and are typical of cumulates derived from calc-alkaline differentiation series, although re-equilibration with trapped and/or percolating melt or fluids may have affected the concentration of the most incompatible and fluid-mobile elements. Because of the cumulate nature of almost all rocks in the pipes, we focus on the mineral chemistry to monitor and understand the fractionation process. The description of the analysed rocks is given in Table 1; analytical methods for the bulk-rocks can be found in the Supplementary Data (SD) Electronic Appendix 1, and rock compositions in SD Electronic Appendix 2.

Table 1: Samples used for trace-element analyses

Sample	Location (N, E)	Type	Magmatic	Sub-solidus
Pipe 1				
P7*†	35°01·010′, 73°42·166′	heterogran. hbl-clinopyroxenite	Cpx–Hbl–Spl	Tr
P10†	35°00·614′, 73°42·147′	fine-grained hbl-clinopyroxenite	Cpx–Hbl–Spl	
P13†	35°00·666′, 73°42·088′	fine-grained hbl-clinopyroxenite	Cpx–Hbl–Spl	
P25†	Boulder	fine-grained hbl-clinopyroxenite	Cpx–Hbl–Spl	Tr
P14†	35°00·666′, 73°42·088′	leucocratic patch	Cpx–Hbl–Ep–Pl?	Ep–Chl–Tr
P1†	35°00·339′, 73°41·805′	fine-grained hbl-clinopyroxenite	Cpx–Hbl–Spl	Chl
P2†	35°00·339′, 73°41·805′	filling of geode	(fluid derived) Cpx–Chl–Ep–TiOx	
P9*	35°00·614′, 73°42·147′	fine-grained clinopyroxenite	Cpx–Hbl–Spl	–
P18*†	35°00·733′, 73°41·927′	fine-grained clinopyroxenite	Cpx–Hbl–Spl	Tr–Serp
P22*	Boulder	coarse dunite-relict Cpx	Ol–Spl (Cpx)	–
P8*	35°01·021′, 73°42·154′	fine-grained leucotonalite	Hbl–Pl–TiOx–Bt?–Grt?	Tr–Ep–Chl–Grt?
Pipe 2				
P42*†	35°03·349′, 73°45·728′	background pyroxenite	Ol–Cpx–Hbl ± Opx–Spl–Grt	–
P47*†	35°03·396′, 73°45·711′	background pyroxenite	Ol–Cpx–Hbl ± Opx–Spl	
P62†	35°04·087′, 73°45·780′	background pyroxenite	Ol–Cpx–Hbl ± Opx–Spl	
P68h†	Boulder	background pyroxenite	Ol–Cpx–Hbl ± Opx–Spl	
P68†	Boulder	leuco-Hbl-gabbro	Hbl–Pl	Grt
P30*	35°03·028′, 73°45·297′	background pyroxenite	Ol–Cpx–Hbl ± Opx	–
P51*	35°03·412′, 73°45·612′	Plag-bearing pyroxenite	Ol–Cpx–Hbl–Opx–Plag–Hcn	–
P52†	35°03·431′, 73°45·565′	Plag-bearing pyroxenite	Ol–Cpx–Hbl–Opx–Plag–Hcn	
P39†	35°03·333′, 73°45·769′	Plag-bearing pyroxenite	Ol–Cpx–Hbl–Opx–Plag–Hcn	
P67†	35°04·087′, 73°45·780′	Hbl-gabbronorite	Opx–Cpx–Hbl–Plag (± Grt?)	Grt?
P64*	35°04·154′, 73°45·633′	dunite	Ol–Cpx	–
P45*	35°03·396′, 73°45·711′	dunite	Ol	Serp
P31*	35°03·017′, 73°45·273′	fine-grained metagabbro	Cpx–Hbl?–Plag? –Ep?	Tr–Ep–Chl
P98†	35°04·022′, 73°45·859′	Hbl-tonalite	Hbl–Plag–TiOx ± Bt? ± Grt?	Chl–Grt–Ep
P63*†	35°04·086′, 73°45·780′	fine-grained leucotonalite	Hbl–Bt–Plag–Ep–Qtz	Tr–Ep

*Bulk-rock.
†Mineral.

Analytical methods

Major element compositions of minerals were determined at ETH Zurich using a JEOL-8200 electron microprobe. Beam conditions were 15 kV and 20 nA, counting times were 40 s on the peak for each element except for Fe and Mn (20 s). *In situ* trace element analyses of opx, cpx, plag, grt, ep and hbl were performed by laser ablation inductively coupled plasma mass spectrometry (LA-ICP-MS) at the University Montpellier II using a single-collector, double-focusing, sector field Element XR (eXtended Range) ICP-MS system, coupled with a Geolas (Microlas) automated platform hosting an ArF 193 nm Compex 102 laser from LambdaPhysik. Ablation experiments were conducted in an ablation cell of *c.* 30 cm^3 in a He atmosphere, which enhances sensitivity and reduces inter-element fractionation (Gunther & Heinrich, 1999). The helium gas stream and particles from the sample were mixed with Ar before entering the plasma. Data were acquired in the fast E-scan mode at low resolution (M/DM = 300). Signals were measured in time-resolved acquisition, devoting 2 min to the blank, and 1 min to the measurement of the sample. The laser was fired using an energy density of 15 J cm^{-2} at a frequency of 10 Hz and using a spot size of 120 μm for opx, plag and ep; and 7 Hz and 77 μm for cpx and hbl. Oxide level, measured using the ThO/Th ratio, was below 0·7%. ^{29}Si was used as an internal standard for ol, opx, plag, grt and hbl; and ^{43}Ca for cpx. Analyte concentrations were calibrated against the NIST 612 rhyolitic glass using the values given by Pearce *et al.* (1997). Data were subsequently reduced using the GLITTER software (van Achterbergh *et al.*, 2001) by carefully inspecting the time-resolved analysis to check for lack of heterogeneity in the analyses.

Mineral chemistry

Pipe 1

Olivines (Table 2, Fig. 8) show a wide range of X_{Mg} [Mg/(Fe + Mg); 0·96–0·85; Fig. 8], NiO (0·03–0·18 wt %) and MnO (0·11–1·11 wt %; Fig. 8). The ol grains with the highest X_{Mg} (≈ 0·96) and MnO and the lowest NiO are non-magmatic secondary grains overgrowing serpentine and calcite. Most ol grains from dunites and olclinopyroxenites have X_{Mg} between 0·85 and 0·90 and NiO between 0·07 and 0·17 wt %, reflecting crystallization from a somewhat already differentiated melt (Fig. 8). Ol from massive dunites with corroded cpx has a similarly low NiO content (∼0·15 wt %) but shows a higher X_{Mg} (≈0·92), consistent with a cpx-undersaturated melt crystallizing olivine and dissolving clinopyroxene.

Clinopyroxene does not show systematic zoning and there is almost no systematic chemical variation between cpx_1 and cpx_2 (Table 3). Magmatic cpx delineates a trend from high X_{Mg} and low Al_2O_3 [X_{Mg} = Mg/(Mg + Fe_{tot}) = 0·93, Al_2O_3 = 0·3 wt %] to lower X_{Mg} and higher Al_2O_3 (X_{Mg} = 0·87, Al_2O_3 = 2·5 wt %; Fig. 9a). TiO_2 is up to 0·2 wt %, increasing with decreasing X_{Mg} (Fig. 9b). Cpx grains with the highest X_{Mg} (0·98–0·94) and lowest Al_2O_3 (0·11–1·3 wt %) and TiO_2 contents are metamorphic. Cpx chromium contents range up to 0·8 wt % and are uncorrelated with X_{Mg}.

Chondrite-normalized rare earth element (REE) patterns (Fig. 10) for magmatic cpx from pyroxenites show flat heavy REE (HREE) segments ($0{\cdot}89 < Dy_N/Lu_N < 1{\cdot}20$), slightly fractionated middle REE (MREE) ($0{\cdot}35 < Sm_N/Dy_N < 0{\cdot}68$) segments and strongly fractionated light REE (LREE) ($0{\cdot}06 < La_N/Sm_N < 0{\cdot}34$) segments. None of the analyzed cpx grains have an Eu anomaly. Cpx_1 shows slight La enrichment, interpreted to represent minute serpentine or chlorite along the cleavage of the analyzed grains (Supplementary Data Electronic Appendix 2). The more primitive the magmatic cpx are (high X_{Mg}, low Al_2O_3 and TiO_2) the less enriched are their normalized REE patterns (Fig. 10). Normalized to primitive mantle (SD Electronic Appendix 2), cpx shows typical arc-signatures, with enrichments in large ion lithophile elements (LILE) and depletions in high field strength elements (HFSE). Cpx from geodes (cpx_g in Figs 9 and 10) is distinct, having the lowest X_{Mg} (0·84–0·88), an average of 1 wt % Al_2O_3, low TiO_2 (0·03 wt %), nearly no chromium and much lower REE contents. These cpx grains crystallized from an aqueous fluid phase, thus having a distinct signature compared with the metamorphic cpx formed during late greenschist-facies recrystallization.

Table 2: Representative analyses of olivine from Pipes 1 and 2

	Pipe 1						Pipe 2	
	Dunite Av.		Overgrowing serp. Av.		Ol-cpxite Av.		Pyroxenite Av.	
	$n = 29$	2σ	$n = 15$	2σ	$n = 26$	2σ	$n = 33$	2σ
SiO_2	39·52	0·46	41·03	0·22	40·11	0·22	37·46	0·84
FeO	8·75	0·27	4·08	0·15	11·27	0·67	18·52	1·22
MnO	0·16	0·02	0·76	0·46	0·19	0·02	0·27	0·03
NiO	0·15	0·01	0·05	0·01	0·14	0·02	0·09	0·02
MgO	50·54	0·45	53·01	0·51	48·66	0·49	43·00	1·03
CaO	0·01	0·01	0·03	0·01	0·01	0·01	0·01	0·01
Total	99·15	0·68	98·97	0·45	100·42	0·32	99·37	1·14
X_{Mg}	0·91	0·00	0·96	0·00	0·88	0·01	0·81	0·01

Euhedral spinels (Table 4) from dunites have cores defining a trend of decreasing X_{Mg} with increasing TiO_2 and Cr# [$0{\cdot}18 < X_{Mg} < 0{\cdot}42$; $0{\cdot}17 < TiO_2 < 0{\cdot}62$ wt %; $0{\cdot}42 < Cr\# = Cr/(Cr + Al + Fe^{3+}) < 0{\cdot}83$]. Anhedral spl from pyroxenites defines a similar trend ($0{\cdot}05 < X_{Mg} < 0{\cdot}52$; $0{\cdot}22 < TiO_2 < 0{\cdot}78$ wt %). The rims of anhedral spl are usually of magnetite with a low TiO_2 content (see SD Electronic Appendix 2).

Amphiboles (Table 5) are dominantly Mg-hbl and tremolite (Fig. 11), the latter often forming rims around cpx and Mg-hbl. The evolution of Mg-hbl towards tremolitic compositions is mostly sharp but occasionally continuous, with Si increasing from 6·85 to 8 a.p.f.u. whereas Na(A) decreases from 0·54 to 0 a.p.f.u. Tremolite represents re-equilibration during the regional greenschist-facies overprint and will not be discussed further. The Mg-hbl ($Si < 7{\cdot}5$ a.p.f.u.) shows an increase of Na_2O and TiO_2 with decreasing X_{Mg} [$Mg/(Mg + Fe_{tot})$] from 0·94 to 0·85 and reflects magmatic processes (Fig. 11). The magmatic character of the Mg-hbl is further indicated by its high Cr_2O_3 content (0·25–1·6 wt %), which decreases with increasing Si content, and its different trace element composition from the metamorphic amphiboles (Fig. 10b). The chondrite-normalized REE patterns of the Mg-hbl are nearly parallel to those of the cpx. In contrast, the REE concentrations in hbl are up to 10 times those of cpx, and increase with decreasing X_{Mg} (Fig. 12a). Normalized to primitive mantle, Mg-hbl shows enrichment in Cs, Pb and Sr with a significant negative Th anomaly (SD Electronic Appendix 2). Only Zr and Hf of the HFSE show depletion compared with adjacent elements.

The rare pegmatitic, leucocratic patches contain two types of amphibole, both overgrown by chlorite: (1)

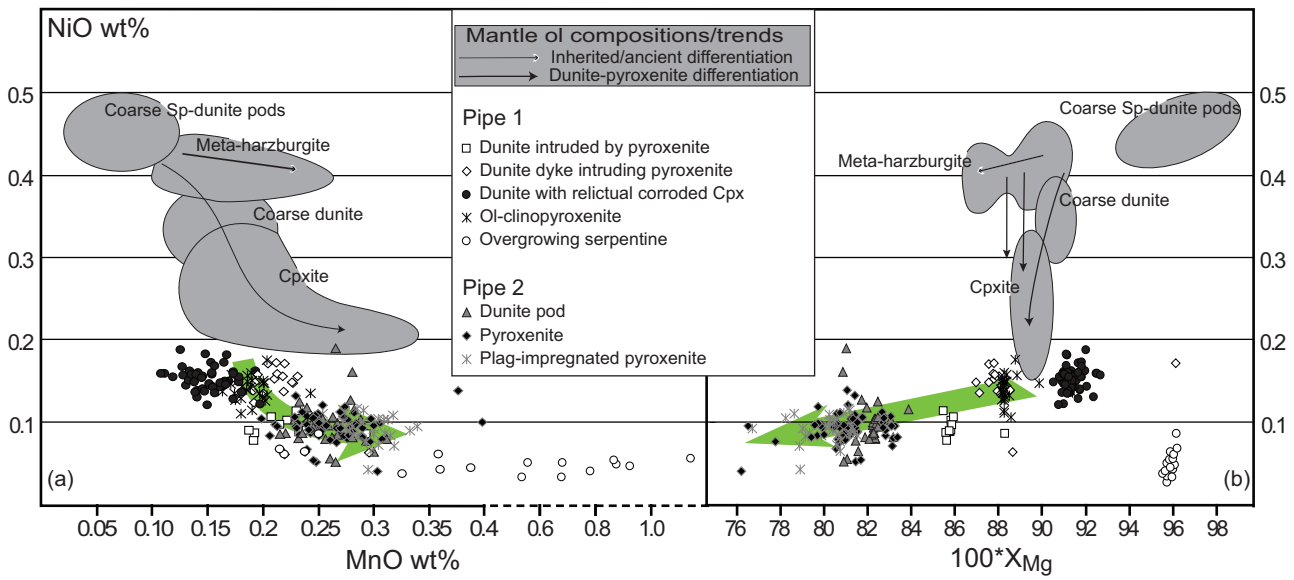

Fig. 8. Pipe 1 and Pipe 2 olivine compositions. Grey fields and mantle differentiation trends of the Sapat mantle rocks are from Bouilhol *et al.* (2009). (a) MnO vs NiO. (b) X_{Mg} vs NiO content. Green arrow reflects the differentiation trend in the crustal pipes.

Table 3: Representative major and trace element analyses of clinopyroxenes from Pipe 1

	Clinopyroxenite									
Sample:	P10		P13		P25		P7	cpx1	P7	cpx2
	Av.	2σ	Av.	2σ	Av.	2σ	Av.	2σ	Av.	2σ
Major elements (wt %)										
	n = 11		*n* = 41		*n* = 48		*n* = 60		*n* = 34	
SiO_2	52·95	0·68	52·52	0·53	53·07	0·48	54·03	0·58	53·76	0·49
TiO_2	0·11	0·05	0·09	0·03	0·07	0·01	0·04	0·01	0·05	0·01
Cr_2O_3	0·24	0·14	0·46	0·08	0·45	0·11	0·54	0·09	0·55	0·08
Al_2O_3	1·72	0·75	1·94	0·37	1·34	0·23	0·89	0·34	1·22	0·39
FeO	3·43	0·27	3·78	0·29	3·57	0·21	2·70	0·19	2·79	0·25
MnO	0·12	0·02	0·13	0·03	0·13	0·02	0·10	0·02	0·09	0·01
NiO	0·01	0·01	0·02	0·01	0·02	0·01	0·02	0·01	0·02	0·01
MgO	16·52	0·27	16·54	0·52	16·78	0·38	17·92	0·39	17·65	0·36
CaO	24·42	0·54	23·42	0·88	23·65	0·56	24·76	0·56	24·82	0·36
Na_2O	0·04	0·03	0·09	0·02	0·07	0·02	0·08	0·02	0·08	0·02
Total	99·58	0·23	99·00	0·54	99·14	0·51	101·08	0·52	101·03	0·44
$X_{Mg}(Fe_{tot})$	0·90	0·01	0·89	0·01	0·89	0·00	0·92	0·01	0·92	0·01
Trace elements (μg g^{-1})										
	n = 4		*n* = 3		*n* = 9		*n* = 14		*n* = 5	
B	3·6	1·0	3·2	3·8	3·2	3·5	17·1	9·0	7·0	1·5
Sc	60·7	11·2	65·1	14·6	67·4	3·9	35·3	1·9	36·6	1·3
V	182·4	48·6	196·5	51·3	152·6	12·0	82·0	9·3	80·3	2·4
Cr	1935·2	625·6	3775·3	532·3	3358·2	630·1	5021·6	1653·0	3460·9	495·3
Mn	1188·1	94·9	998·6	65·7	989·0	65·2	870·9	105·4	789·4	31·4
Co	39·1	4·7	35·8	3·0	33·0	2·1	34·4	6·0	30·6	1·0
Ni	102·9	14·6	125·5	14·1	140·1	20·2	234·2	37·2	180·7	2·4
Cu	0·163	0·209	1·12	1·79	0·55	1·07	0·82	1·49	0·062	0·005
Zn	19·4	3·3	14·2	1·6	12·3	0·8	30·0	55·2	6·9	0·9
Li	2·51	0·60	2·6	0·7	1·9	0·2	1·9	0·3	2·0	0·3
Mo	0·029	0·012	0·023	1/3	0·035	0·025	0·123	0·044	0·062	1/5
Cs	0·27	0·28	0·26	0·36	0·07	0·06	0·44	0·27	0·03	0·02
Rb	0·89	1·32	0·06	0·03	0·02	0·00	0·07	0·03	0·02	0·01
Ba	2·50	3·13	0·27	0·36	0·19	0·18	0·84	0·61	0·17	0·08
Th	0·0076	0·0023	0·0004	0·0004	0·0009	0·0008	0·0003	0·0001	0·0013	0·0016
U	0·0483	0·0631	0·0001	0·0001	0·1071	0·3014	0·0016	0·0015	0·0004	0·0003
Nb	0·0144	0·0104	0·0027	0·0001	0·0026	0·0007	0·0050	0·0018	0·0057	0·0031
Ta	0·0043	0·0019	0·0010	1/3	0·0015	0·0007	0·0031	0·0016	0·0020	1/5
La	0·063	0·006	0·031	0·011	0·011	0·002	0·025	0·013	0·010	0·004
Ce	0·213	0·022	0·098	0·033	0·048	0·008	0·037	0·007	0·033	0·005
Pb	0·138	0·070	0·076	0·046	0·029	0·010	0·017	0·004	0·024	0·003
Pr	0·042	0·009	0·023	0·011	0·011	0·002	0·008	0·002	0·007	0·001
Sr	7·79	1·76	3·63	0·22	3·15	0·16	3·32	0·30	3·09	0·07
Nd	0·263	0·063	0·150	0·051	0·091	0·023	0·064	0·015	0·061	0·004
Sm	0·162	0·037	0·114	0·040	0·067	0·019	0·047	0·015	0·034	0·003
Zr	1·066	0·233	0·313	0·143	0·200	0·163	0·054	0·008	0·049	0·005
Hf	0·058	0·017	0·023	0·011	0·012	0·006	0·003	0·001	0·005	0·003
Eu	0·084	0·019	0·055	0·013	0·036	0·006	0·023	0·005	0·017	0·006
Gd	0·317	0·087	0·208	0·073	0·151	0·036	0·093	0·014	0·086	0·014
Tb	0·065	0·020	0·044	0·014	0·033	0·008	0·018	0·003	0·019	0·002
Dy	0·481	0·162	0·351	0·125	0·263	0·065	0·149	0·019	0·132	0·011
Y	2·68	0·84	1·92	0·59	1·44	0·34	0·84	0·10	0·75	0·04
Ho	0·105	0·035	0·079	0·027	0·060	0·016	0·032	0·006	0·027	0·002
Er	0·322	0·109	0·250	0·099	69·668	0·038	0·094	0·013	0·091	0·009
Ti	937·1	315·2	649·7	246·9	395·0	73·5	271·0	23·3	257·2	12·2
Tm	0·048	0·016	0·037	0·012	0·027	0·006	0·015	0·002	0·012	0·003
Yb	0·329	0·104	0·237	0·078	0·173	0·040	0·105	0·019	0·088	0·015
Lu	0·049	0·014	0·032	0·010	0·025	0·004	0·014	0·003	0·013	0·002

(continued)

Table 3: Continued

Sample:	Clinopyroxenite				Filling geodes	
	P18		P1	cpx2	P2	Cpxg
	Av.	2σ	Av.	2σ	Av.	2σ
Major elements (wt %)	$n=28$		$n=45$		$n=16$	
SiO_2	53·15	1·16	53·26	0·69	53·38	0·28
TiO_2	0·04	0·01	0·07	0·01	0·03	0·04
Cr_2O_3	0·40	0·18	0·33	0·06	0·03	0·02
Al_2O_3	1·07	0·41	1·39	0·18	0·88	0·39
FeO	2·04	0·67	3·09	0·18	4·59	0·84
MnO	0·11	0·03	0·11	0·02	0·28	0·12
NiO	0·02	0·01	0·02	0·01	0·01	0·01
MgO	18·42	1·53	16·73	0·78	14·88	0·52
CaO	23·69	1·41	23·84	0·47	24·51	0·30
Na_2O	0·05	0·03	0·08	0·01	0·37	0·15
Total	99·00	1·16	98·92	1·10	98·98	0·28
$X_{Mg}(Fe_{tot})$	0·92	0·02	0·91	0·01	0·85	0·03
Trace elements (μg g^{-1})	$n=5$		$n=6$		$n=8$	
B	13·5	6·8	7·0	0·5	2·8	0·8
Sc	56·5	11·0	60·2	3·4	96·9	177·9
V	115·6	21·7	163·3	10·1	174·4	65·5
Cr	3907·2	273·0	2632·3	655·3	325·7	306·1
Mn	902·5	63·5	890·0	27·7	1962·4	393·0
Co	26·3	1·4	37·7	2·7	22·0	1·6
Ni	138·9	11·4	154·4	19·0	25·3	8·7
Cu	0·4	0·2	46·9	114·2	0·8	1·4
Zn	9·8	1·9	16·1	2·3	22·8	2·0
Li	3·2	0·3	2·6	0·2	6·2	2·8
Mo	0·018	0·007	0·101	0·021	0·032	0·019
Cs	0·04	0·06	0·30	0·25	1·62	3·57
Rb	0·02	0·02	0·18	0·27	1·59	3·47
Ba	0·10	0·09	1·33	1·01	0·63	1·16
Th	0·0011	0·0012	0·0008	0·0002	0·0005	0·0003
U	0·0002	0·0001	0·0009	0·0004	0·0197	0·0380
Nb	0·0026	0·0008	0·0042	0·0017	0·0207	0·0281
Ta	0·0010	1/5	0·0020	0·0008	0·0025	0·0016
La	0·010	0·001	0·071	0·023	0·008	0·007
Ce	0·040	0·008	0·103	0·012	0·131	0·324
Pb	0·022	0·004	0·069	0·019	0·044	0·056
Pr	0·010	0·003	0·027	0·004	0·009	0·014
Sr	3·06	0·44	4·24	0·19	5·79	0·37
Nd	0·072	0·011	0·163	0·025	0·018	0·032
Sm	0·051	0·008	0·080	0·017	0·011	0·010
Zr	0·118	0·050	0·178	0·019	1·371	2·192
Hf	0·007	0·005	0·009	0·006	0·041	0·064
Eu	0·026	0·002	0·038	0·007	0·007	0·014
Gd	0·105	0·012	0·165	0·021	0·013	0·014
Tb	0·024	0·003	0·034	0·004	0·002	0·002
Dy	0·189	0·021	0·270	0·038	0·013	0·017
Y	1·04	0·11	1·64	0·22	0·09	0·09
Ho	0·043	0·004	0·061	0·006	0·004	0·004
Er	0·125	0·013	0·185	0·027	0·015	0·014
Ti	329·4	35·9	539·4	36·6	205·2	124·4
Tm	0·019	0·003	0·028	0·006	0·005	0·003
Yb	0·131	0·017	0·181	0·024	0·046	0·046
Lu	0·019	0·001	0·027	0·004	0·021	0·026

large, millimeter-sized edenite with a high TiO_2 content (0·25–0·36 wt %), often rimmed by (2) pargasite with low TiO_2 (0·15 wt %). These amphiboles are much more enriched in K_2O (0·14–0·46 wt %) than any other amphiboles found in Pipe 1. Edenitic amphiboles within the leucocratic patches show similar but 20 times more enriched chondrite-normalized REE patterns than Mg-hbl (Fig. 10). In addition, edenite shows a pronounced negative Eu anomaly (Eu* ≈ 0·7). Normalized to primitive mantle, edenite shows enrichment in Cs, but not in Pb,

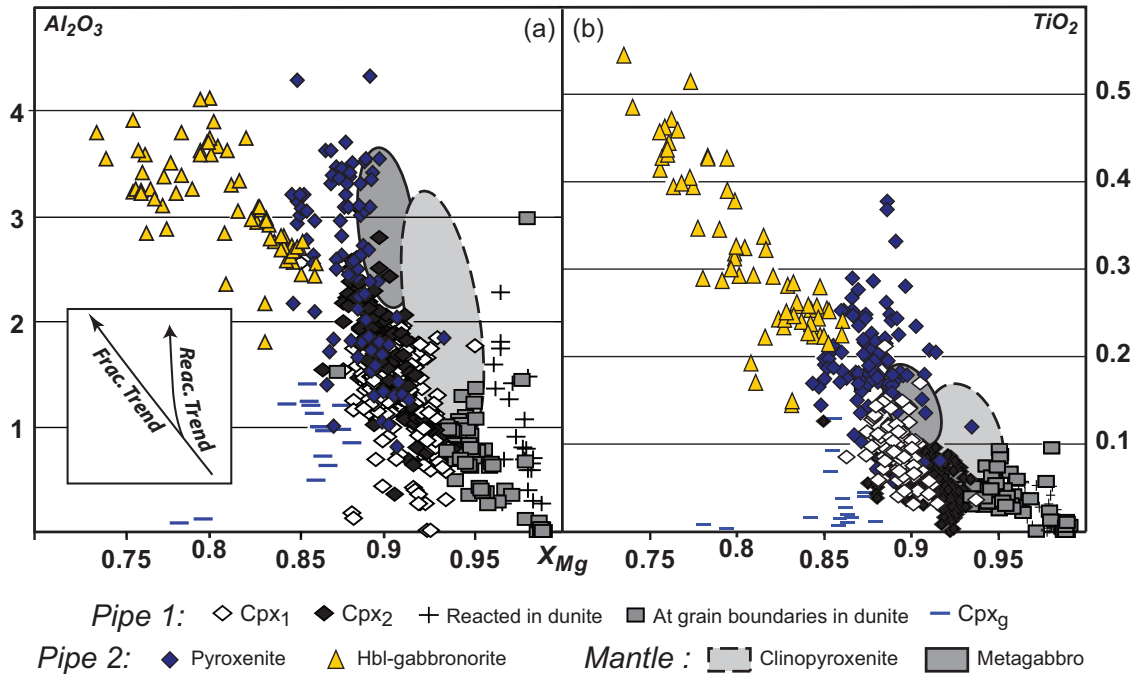

Fig. 9. Compositional range of cpx in Pipes 1 and 2 showing the evolution of X_{Mg} vs (a) Al_2O_3 and (b) TiO_2. Cpx_g indicates clinopyroxene in geodes of Pipe 1 (Fig. 4a). Cpx from olivine-clinopyroxenite, clinopyroxenite and metagabbros of the mantle section are plotted for comparison.

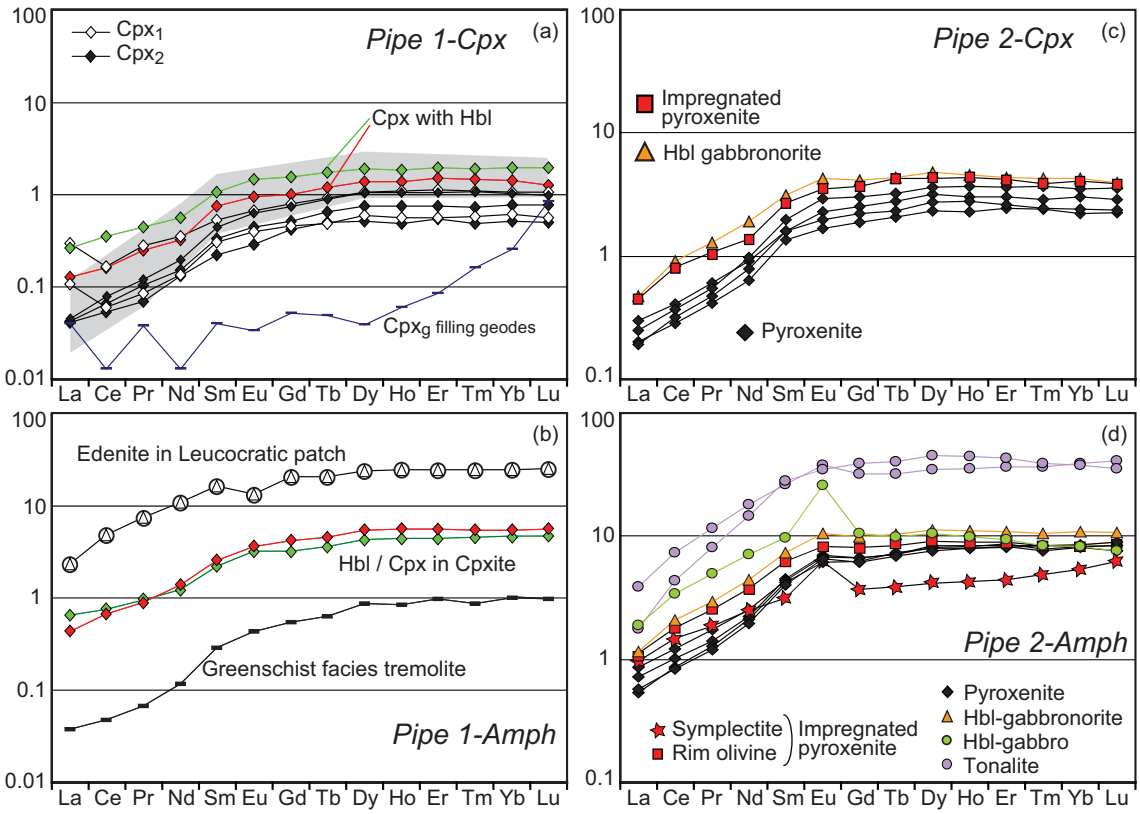

Fig. 10. Chondrite-normalized REE patterns of cpx and amphibole. (a) Cpx in Pipe 1. Grey field represents cpx in the mantle rocks (Bouilhol *et al.*, 2009). (b) Amphiboles in Pipe 1. The distinction between late sub-solidus amphibole (tremolite pseudomorphs after cpx) and magmatic amphibole is clear. The red and green symbols correspond to samples P10 and P13, respectively, in which hbl and cpx are in equilibrium. (c) Cpx in Pipe 2. (d) Amphiboles from Pipe 2. Normalization values from Sun & McDonough (1989).

Table 4: Representative analyses of spinel from Pipes 1 and 2

	Pipe 1				Pipe 2			
	P22 Dunite Av.		P7 Cpxite Av.		Pyroxenite Spinel Av.		Hercynite Av.	
	$n = 19$	2σ	$n = 10$	2σ	$n = 19$	2σ	$n = 15$	2σ
SiO_2	0·02	0·03	0·02	0·01	0·00	0·00	0·03	0·08
TiO_2	0·18	0·01	0·30	0·12	0·11	0·04	0·01	0·01
Cr_2O_3	55·40	1·65	40·33	3·60	12·12	1·23	0·41	1·47
Al_2O_3	10·04	1·74	14·23	2·03	48·04	2·21	64·62	2·61
FeO	26·72	1·39	41·43	4·90	27·61	1·92	17·36	0·91
MnO	0·50	0·11	1·42	0·47	0·23	0·02	0·12	0·02
NiO	0·01	0·01	0·05	0·01	0·09	0·02	0·11	0·03
MgO	8·00	0·88	3·03	1·60	11·42	0·79	16·66	0·64
Total	100·90	0·28	101·10	0·90	99·66	0·50	99·46	0·71
X_{Mg}	0·39	0·04	0·15	0·07	0·48	0·03	0·64	0·02
Cr#	0·73	0·03	0·53	0·03	0·14	0·02	0·00	0·02

and strong negative Sr, Th, Ti, Zr, and Hf anomalies, whereas Nb shows a slight positive anomaly compared with Ta and especially Th.

Epidote in the leucocratic patches shows oscillatory zoning in FeO (3·1–6·6 wt %) and MnO (0·03–0·32 wt %) contents (SD Electronic Appendix 2); $X_{Epidote}$ [$Fe^{3+}/(Fe^{3+} + Al^{3+} + Cr^{3+})$] varies from 0·20 to 0·44, with Mn-poor epidote having the lowest X_{Ep}. Mn–Fe-rich epidotes have chondrite-normalized REE patterns similar to those of plag, with a significant positive Eu anomaly ($Eu^* \approx 13·5$; SD Electronic Appendix 2), pointing to a magmatic origin (e.g. Frei *et al.*, 2004). Mn-poor epidote is much poorer in REE, and its REE patterns differ from those of Mn-rich epidote in having a fractionated MREE–HREE segment ($Gd_N/Lu_N \approx 0·1$) and a smaller Eu anomaly, pointing to a metamorphic origin.

Pipe 2

Olivine compositions have $X_{Mg} = 0·76$–$0·84$ and NiO contents from 0·04 to 0·20 wt % (Fig. 8; Table 2). The MnO content is high (0·21–0·40 wt %). Pipe 1 and Pipe 2 olivines together define a differentiation trend along which NiO and X_{Mg} decrease concomitantly.

Clinopyroxenes from pyroxenites (Table 6) have X_{Mg} of 0·85–0·91 with a wide range in Al_2O_3 (0·8–4·3 wt %), TiO_2 ($\leq$0·38 wt %) and Cr_2O_3 ($\leq$0·5 wt %) contents (Fig. 9). Al and Ti contents increase with decreasing X_{Mg}, whereas Cr contents are uncorrelated. The most primitive cpx compositions overlap with those of the most differentiated cpx in Pipe 1. Cpx grains from more differentiated rocks (i.e. hbl-gabbronorite) are different. Al_2O_3 contents increase from 2·5 to 4·1 wt % with X_{Mg} decreasing from 0·86 to 0·79 for cpx in the dyke walls, whereas cpx inside the dyke show a decrease to 2·1 wt % Al_2O_3 with X_{Mg} further decreasing to 0·67. Whereas Al_2O_3 starts decreasing at $X_{Mg} = 0·79$, TiO_2 increases from 0·2 to 0·5 wt % with X_{Mg} decreasing to 0·74 and then drops drastically to $TiO_2 \approx 0·1$ wt % at $X_{Mg} = 0·7$. The Cr_2O_3 content decreases from 0·3 wt % at $X_{Mg} = 0·86$ to the detection limit at $X_{Mg} = 0·7$.

Chondrite-normalized REE patterns of magmatic cpx have flat HREE ($0·93 < Dy_N/Lu_N < 1·32$) segments, slightly fractionated MREE segments ($0·43 < Sm_N/Dy_N < 0·69$) without an Eu anomaly, and strongly fractionated LREE ($0·11 < La_N/Sm_N < 0·28$; Fig. 10) segments. Cpx REE concentrations increase with decreasing X_{Mg} (Fig. 12a). Normalized to primitive mantle, cpx shows a strong negative Zr, Hf and Nb anomaly and Ta is decoupled from Nb with sub-chondritic Nb/Ta ratios. Cpx grains from pyroxenite have positive Pb and Sr anomalies. Cpx grains from hbl-gabbronorite dykes have no Pb anomaly and a small negative Sr anomaly.

Amphiboles have pargasitic to tremolitic compositions (Fig. 11; Table 7) and the distinction between magmatic and metamorphic amphibole is again largely based on textures and mineral chemistry. Amphiboles replacing cpx in pyroxenites, in coarse-grained reaction rims around ol and in the hbl-gabbros are Mg-hbl to tschermakite. Magmatic amphiboles in the hbl-gabbronorite and in the late tonalitic dykes are edenite to pargasite. From pyroxenites to hbl-gabbronorite, Ti and Na contents in magmatic amphiboles increase [$0·1 < Na(A) < 0·8$; $0 < Ti$ p.f.u $< 0·2$] with decreasing X_{Mg} (from 0·93 to 0·70; Fig. 11b and c), similar to hbl in Pipe 1. In contrast, in the hbl-gabbronorite to tonalitic dykes the Na content decreases [$0·55 < Na(A) < 0·8$] and Ti stays constant with decreasing X_{Mg} ($0·33 < X_{Mg} < 0·68$). This chemical evolution is expected from amphiboles crystallizing from evolving magmas (e.g. Cawthorn & O'Hara, 1976). Bluish-green amphiboles replacing plag are pargasitic, with low Si and high Na(A) content and Ti below detection limit. These amphiboles are related to high-temperature fluid re-equilibration, and contrast with secondary greenschist-facies tremolite.

Normalized to chondrite, magmatic amphiboles in the pyroxenites have flat HREE segments ($0·82 < Dy_N/Lu_N < 1·17$), slightly fractionated MREE ($0·46 < Sm_N/Dy_N < 0·71$) segments and strongly fractionated LREE segments ($0·12 < La_N/Sm_N < 0·30$; Fig. 10). Hbl from symplectites between ol and plag in the impregnated

Table 5: Representative major and trace element analyses of amphibole from Pipe 1

	Clinopyroxenite						Leucocratic patch	
Sample:	P10		P13		P25		P14	
	Av.	2σ	Av.	2σ	Av.	2σ	Av.	2σ
Major elements (wt %)	*n* = 11		*n* = 36		*n* = 23		*n* = 14	
SiO_2	50·52	1·45	50·01	1·58	56·61	1·21	47·28	0·95
TiO_2	0·23	0·07	0·23	0·07	0·03	0·04	0·32	0·05
Cr_2O_3	0·43	0·17	0·94	0·46	0·15	0·12	0·08	0·02
Al_2O_3	6·81	1·57	6·79	1·86	0·65	1·06	6·94	0·88
FeO	5·37	0·47	5·45	1·17	3·57	0·57	11·30	1·56
MnO	0·09	0·02	0·10	0·04	0·13	0·03	0·29	0·07
NiO	0·02	0·02	0·03	0·01	0·03	0·01	0·01	0·01
MgO	19·01	0·75	18·95	0·73	22·26	0·77	15·27	1·13
CaO	12·60	0·18	12·38	0·24	12·84	0·66	11·26	0·60
Na_2O	1·28	0·32	1·33	0·38	0·17	0·15	2·09	0·14
K_2O	0·10	0·08	0·01	0·01	0·01	0·01	0·19	0·05
Total	96·46	0·20	96·22	0·45	98·65	0·40	97·01	0·86
X_{Mg}	0·87	0·02	0·88	0·02	0·93	0·02	0·71	0·04
NaK (A)	0·37	0·10	0·37	0·11	0·05	0·04	0·64	0·05
Trace elements (μg g^{-1})	*n* = 4		*n* = 5		*n* = 1		*n* = 2	
B	4·5	2·1	3·3	1·4	202·0		2·9	0·3
Sc	70·5	1·9	110·9	4·8	50·0		116·3	23·5
V	304·8	12·7	496·2	60·4	98·2		436·5	144·3
Cr	3130·2	440·4	6636·7	816·8	4702·9		633·8	184·4
Mn	737·5	84·8	799·0	74·9	1998·3		1955·5	114·2
Co	58·4	1·4	55·1	3·4	117·7		65·6	0·9
Ni	202·0	12·7	212·7	16·6	497·1		60·3	0·8
Cu	0·1	0·0	2·2	1·7	64·7		11·9	8·9
Zn	28·9	2·6	21·9	2·1	35·6		96·0	1·2
Li	7·5	3·0	4·8	3·6	1·4		3·8	0·8
Mo	0·077	0·027	0·044	0·009	0·053		0·025	1/2
Cs	0·277	0·301	0·122	0·051	2·020		0·327	0·002
Rb	2·66	0·56	1·84	0·40	0·45		0·45	0·13
Ba	17·63	7·61	15·26	7·08	7·48		2·60	0·68
Th	0·0223	0·0150	0·0015	0·0004	0·0076		0·0027	0·0010
U	0·0320	0·0375	0·0017	0·0007	0·0300		0·0024	0·0009
Nb	0·1308	0·0289	0·1208	0·0401	0·0056		0·5055	0·0431
Ta	0·0065	0·0029	0·0036	0·0015	<0·0010		0·0128	0·0035
La	0·15	0·02	0·12	0·01	0·01		0·55	0·04
Ce	0·46	0·09	0·47	0·06	0·03		2·94	0·00
Pb	0·43	0·04	0·24	0·05	0·08		0·21	0·00
Pr	0·09	0·02	0·10	0·01	0·01		0·71	0·07
Sr	22·7	4·9	11·0	1·5	7·5		9·0	1·9
Nd	0·572	0·051	0·747	0·086	0·054		5·030	0·990
Sm	0·338	0·036	0·447	0·066	0·044		2·468	0·809
Zr	2·17	0·66	2·16	0·25	0·09		10·06	0·74
Hf	0·121	0·014	0·121	0·024	0·006		0·568	0·021
Eu	0·187	0·004	0·237	0·027	0·025		0·762	0·158
Gd	0·663	0·026	0·972	0·104	0·112		4·143	1·694
Tb	0·135	0·007	0·190	0·020	0·024		0·763	0·328
Dy	1·076	0·064	1·531	0·154	0·220		5·980	2·376
Y	6·238	0·151	8·928	0·943	1·217		34·57	12·91
Ho	0·250	0·006	0·349	0·035	0·048		1·352	0·540
Er	0·735	0·056	1·062	0·096	0·159		4·040	1·471
Ti	2073	108	2843	529	196		6065	3254
Tm	0·11	0·01	0·16	0·02	0·02		0·61	0·20
Yb	0·78	0·03	1·03	0·08	0·17		4·12	1·15
Lu	0·12	0·01	0·16	0·02	0·02		0·64	0·14

zones has a slightly fractionated MREE–HREE segment ($0{\cdot}44 < Dy_N/Sm_N < 0{\cdot}56$), a positive Eu anomaly ($Eu^* = 1{\cdot}6$–2), and a fractionated LREE segment ($0{\cdot}13 < La_N/Sm_N < 0{\cdot}16$). In some cases hbl rimming ol has trace-element concentrations similar to magmatic amphibole (i.e. a flat HREE segment, a steep fractionated LREE segment and no Eu anomaly), thus indicating different equilibria leading to the formation of peritectic hbl around ol and leading to the symplectitic hbl. Normalized to primitive mantle, Ti in pyroxenite hbl

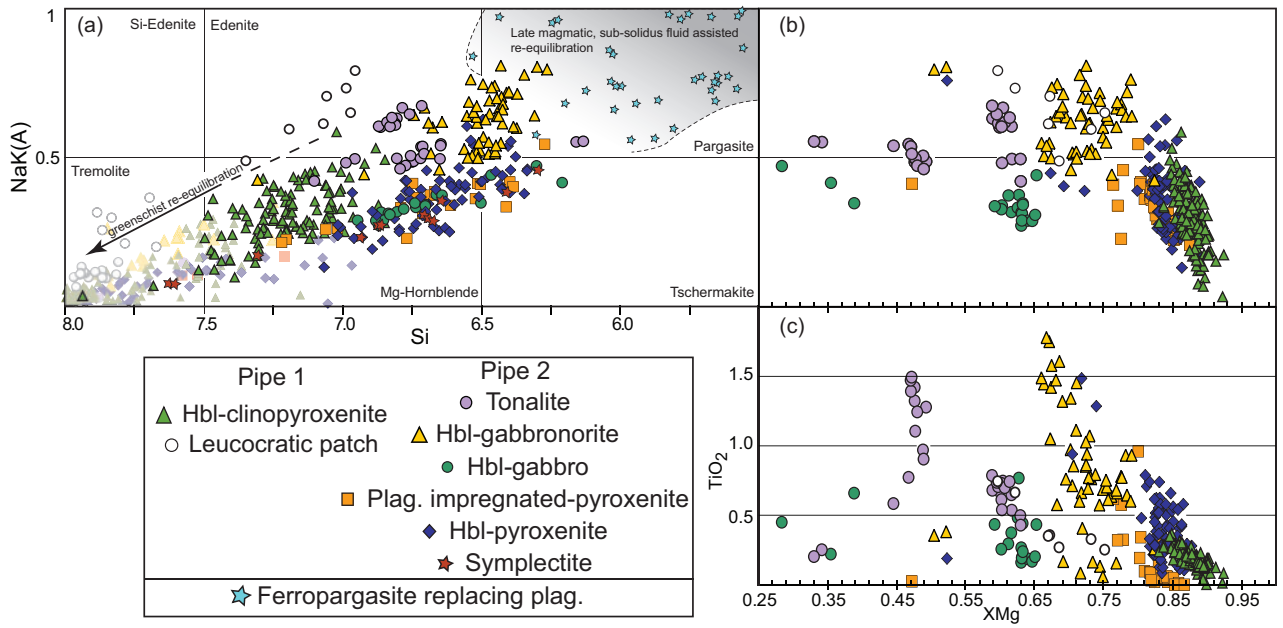

Fig. 11. (a) Leake classification diagram for amphiboles from Pipes 1 and 2 (recalculated assuming no Na on the M4 site). Magmatic amphiboles are shown as dark shaded symbols; metamorphic amphiboles are pale shaded. Ferropargasite is present in plag-bearing lithologies of both pipes, and represents high-temperature re-equilibration in the presence of a fluid phase. Discrimination between magmatic and metamorphic amphiboles is mainly based on textural observations; equilibration in sub-solidus conditions leads to a continuum in the observed compositions. (b) X_{Mg} vs Na + K in the A site for magmatic hbl. (c) X_{Mg} vs TiO_2 (wt %) content of magmatic hbl.

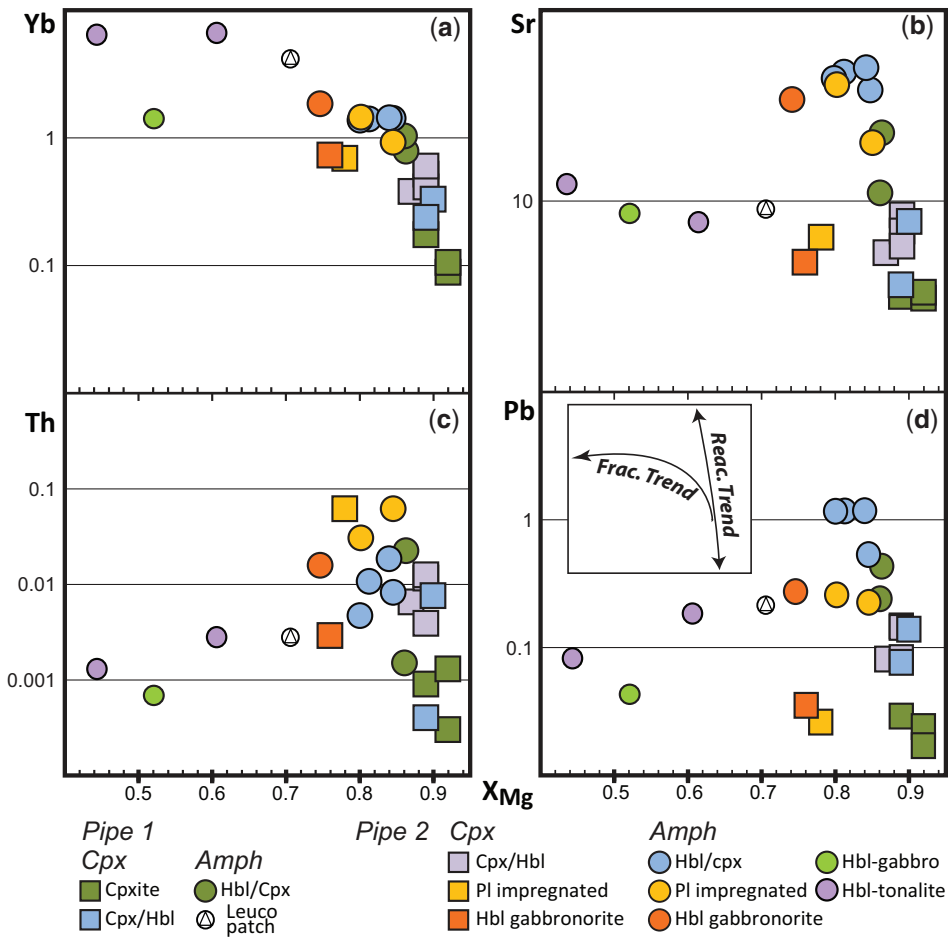

Fig. 12. Cpx and amph X_{Mg} evolution vs (a) Yb, (b) Sr, (c) Th and (d) Pb. All trace element abundances in ppm.

Table 6: Representative major and trace element analyses of clinopyroxene from Pipe 2

	Pyroxenite							
Sample:	P42		P47		P68		P62	
	Av.	2σ	Av.	2σ	Av.	2σ	Av.	2σ
Major elements (wt %)	$n=26$		$n=23$		$n=7$		$n=22$	
SiO_2	52·26	0·62	52·27	0·76	51·98	0·72	52·68	0·90
TiO_2	0·18	0·06	0·19	0·05	0·14	0·02	0·19	0·07
Cr_2O_3	0·30	0·12	0·23	0·12	0·28	0·17	0·18	0·14
Al_2O_3	2·49	0·68	2·37	0·92	2·78	0·70	2·28	0·81
FeO	4·19	0·69	3·73	0·27	3·74	0·32	3·62	0·47
MnO	0·13	0·03	0·12	0·01	0·13	0·02	0·13	0·03
NiO	0·00	0·01	0·01	0·01	0·01	0·02	0·02	0·01
MgO	16·34	0·72	16·33	0·58	16·23	0·23	16·23	0·49
CaO	24·15	1·20	24·28	0·63	24·15	0·56	24·49	0·66
Na_2O	0·08	0·03	0·05	0·02	0·12	0·09	0·04	0·03
Total	100·13	0·58	99·59	0·39	99·58	0·48	99·87	0·73
$X_{Mg}(Fe_{tot})$	0·87	0·02	0·89	0·01	0·89	0·01	0·89	0·02
Trace elements (μg g^{-1})	$n=3$		$n=7$		$n=3$		$n=3$	
B	4·0	0·3	4·6	0·6	3·3	0·1	1·6	1/3
Sc	94·4	16·2	102·8	4·5	103·6	0·4	115·8	1·7
V	265·6	45·3	298·2	31·5	281·3	2·4	325·7	4·8
Cr	2748·3	326·2	2967·8	724·5	3282·8	105·5	3203·5	527·5
Mn	1224·4	180·8	1096·3	106·8	1015·5	25·1	1175·6	30·2
Co	45·6	10·3	37·6	4·2	32·3	2·1	31·7	0·3
Ni	120·1	12·1	127·2	21·7	119·7	6·0	99·2	2·9
Cu	28·8	40·4	4·8	7·2	14·4	16·5	b.d.	
Zn	26·9	8·9	16·7	3·5	12·6	2·2	14·0	3·1
Li	1·0	0·3	0·9	0·4	0·8	0·1	1·4	0·1
Mo	0·034	1/3	0·110	0·001	0·059	1/3	<0·05	
Cs	<0·005		0·040	0·001	0·010	0·004	0·007	1/3
Rb	<0·009		1·108	1·872	0·010	0·000	<0·012	
Ba	0·009	0·002	0·714	1·360	0·044	1/3	0·016	1/3
Th	0·0065	0·0024	0·0116	0·0086	0·0039	0·0035	0·0125	0·0043
U	0·0023	0·0007	0·0041	0·0022	0·0013	0·0010	0·0052	0·0029
Nb	0·0028	0·0013	0·0424	0·0573	0·0036	1/3	<0·003	
Ta	<0·0006		0·0062	0·0039	0·0007	1/3	<0·002	
La	0·048	0·014	0·071	0·022	0·046	0·002	0·059	0·005
Ce	0·175	0·057	0·251	0·058	0·197	0·005	0·227	0·010
Pb	0·081	0·038	0·147	0·044	0·143	0·010	0·083	0·019
Pr	0·039	0·012	0·058	0·013	0·045	0·005	0·053	0·002
Sr	5·35	1·77	8·42	3·39	6·95	0·13	5·78	0·40
Nd	0·298	0·074	0·426	0·084	0·370	0·048	0·456	0·032
Sm	0·207	0·072	0·244	0·083	0·244	0·012	0·305	0·002
Zr	0·751	0·199	1·366	0·362	0·870	0·038	1·067	0·037
Hf	0·039	0·007	0·059	0·027	0·060	0·003	0·076	0·004
Eu	0·098	0·033	0·134	0·027	0·115	0·006	0·170	0·005
Gd	0·385	0·111	0·521	0·194	0·456	0·038	0·620	0·054
Tb	0·078	0·026	0·105	0·036	0·087	0·004	0·121	0·001
Dy	0·594	0·183	0·808	0·208	0·701	0·011	0·916	0·008
Y	3·195	1·025	4·313	1·167	3·727	0·129	4·900	0·207
Ho	0·130	0·044	0·172	0·044	0·157	0·008	0·210	0·008
Er	0·404	0·115	0·498	0·113	0·437	0·034	0·600	0·047
Ti	1155	261	1772	283	1237	30·9	1811	10·3
Tm	0·061	0·018	0·074	0·022	0·062	0·004	0·094	0·006
Yb	0·379	0·119	0·516	0·163	0·411	0·012	0·599	0·028
Lu	0·057	0·018	0·073	0·024	0·061	0·002	0·091	0·003

(continued)

Table 6: Continued

Sample:	Impreg. pxt P39	Hbl-gabbronorite P67	
	Av.	Av.	2σ
Major elements (wt %)	$n=1$	$n=45$	
SiO_2	51·45	51·28	0·27
TiO_2	0·43	0·44	0·04
Cr_2O_3	0·07	0·07	0·03
Al_2O_3	3·41	3·36	0·29
FeO	7·09	7·81	0·54
MnO	0·21	0·23	0·02
NiO	0·00	0·00	0·00
MgO	14·39	14·01	0·40
CaO	22·59	22·43	1·18
Na_2O	0·24	0·26	0·06
Total	99·88	99·91	0·40
$X_{Mg}(Fe_{tot})$	0·78	0·76	0·01
Trace elements (μg g^{-1})	$n=1$	$n=2$	
B	1·0	1·0	0·04
Sc	120·5	114·2	0·1
V	324·9	322·1	4·4
Cr	2584·3	1697·9	68·9
Mn	1453·1	1508·5	89·9
Co	41·4	43·8	2·8
Ni	104·4	71·7	0·4
Cu	<0·041	<0·041	
Zn	26·0	30·6	3·2
Li	0·5	0·8	0·1
Mo	<0·059	<0·055	
Cs	<0·0071	0·007	½
Rb	<0·0138	<0·0132	
Ba	0·014	<0·0119	
Th	0·0615	0·0029	0·0000
U	0·0166	0·0022	0·0001
Nb	<0·0039	0·0038	½
Ta	0·0036	<0·0024	
La	0·108	0·112	0·013
Ce	0·498	0·559	0·079
Pb	0·026	0·034	0·002
Pr	0·103	0·123	0·022
Sr	6·43	4·76	0·27
Nd	0·642	0·890	0·160
Sm	0·416	0·482	0·021
Zr	2·117	1·581	0·371
Hf	0·070	0·085	0·021
Eu	0·203	0·249	0·044
Gd	0·762	0·847	0·126
Tb	0·159	0·163	0·025
Dy	1·096	1·230	0·144
Y	5·940	6·350	1·047
Ho	0·246	0·259	0·040
Er	0·703	0·725	0·141
Ti	1862	1714	178·6
Tm	0·100	0·110	0·022
Yb	0·688	0·729	0·099
Lu	0·099	0·100	0·017

b.d., below detection limit.

has either a slight positive or a negative anomaly (SD Electronic Appendix 2).

Edenite in the hbl-gabbronorite shows the same REE pattern as hbl in the pyroxenites, but has higher REE concentrations. Hbl in hbl-gabbro dyke margins and hbl inclusions in plag within these dykes have flat MREE–HREE segments, a strong Eu anomaly (Eu* ≈ 2·5), and fractionated LREE segments, the latter being the most enriched of all amphiboles in the mafic lithologies of Pipe 2. Magmatic edenite in the tonalites has the highest REE concentrations, a flat MREE–HREE segment up to 45 times chondrite, and a steep fractionated LREE segment. Normalized to primitive mantle, all amphiboles have a pronounced negative Zr–Hf anomaly (SD Electronic Appendix 2). Hbl in the hbl-gabbronorite dykes and dyke margins and edenite from the tonalites have negative Ti anomalies. Pb and Sr show strong positive anomalies in hbl from pyroxenite, whereas Sr shows a smaller positive anomaly in hbl from the infiltrated pyroxenites and in the hbl-gabbronorites. In the most differentiated rocks (hbl-gabbronorite and tonalite) Pb is slightly depleted, whereas Sr shows a strong negative anomaly. Rb, Ba and Th and U are more enriched in hbl from the pyroxenites than from the differentiated rocks.

Orthopyroxenes from the ol-clinopyroxenite have high X_{Mg} (0·88–0·82) and Al_2O_3 contents between 2·4 and 3·3 wt % (Fig. 13, Table 8), low TiO_2 (approximately at the detection limit) and Cr_2O_3 up to 0·27 wt %. Opx grains in the infiltrated pyroxenites, from symplectites and rimming ol against plag, have a restricted range in X_{Mg} (0·80–0·84) and have Al_2O_3 contents varying from 1·8 to 3·8 wt % with insignificant Cr and Ti. Opx from the hbl-gabbronorite has a wide range of X_{Mg} (0·63–0·79), a decrease in Al_2O_3 from 3·1 to 1·9 wt % and Cr_2O_3 contents decreasing from 0·24 to 0·01 wt % with decreasing X_{Mg}, whereas TiO_2 increases from 0·05 to 0·21 wt %.

Normalized to chondrite, opx has a regular fractionated REE pattern, with La_N/Lu_N varying from 0·002 to 0·024 (Fig. 13). Opx grains from peritectic reactions in the pyroxenites have the highest REE concentrations, with Lu_N up to 10·8 times chondrite. Opx rimming ol against plag in infiltrated pyroxenites has a different pattern, with fractionated HREE segments ($0{\cdot}03 < Dy_N/Lu_N < 0{\cdot}71$), and rather flat MREE–LREE segments ($0{\cdot}34 < La_N/Dy_N < 8{\cdot}61$).

Spl inclusions in ol and spl grains in pyroxenites (Table 4) show a wide range of X_{Mg}, Cr, Ti and Al contents, with a general trend of decreasing X_{Mg} (from 0·62 to 0·24) with increasing TiO_2 (0·5–1·35 wt %) and Cr# (0·06–0·25) (Supplementary Data Electronic Appendix 2). Green spl, either found with garnet at grain boundaries within the pyroxenite groundmass or associated with hbl and opx and occurring in symplectites, is hercynite. Ilmenite is the opaque phase in the most differentiated rocks.

Garnets of various types are found within Pipe 2. In the pyroxenites, garnets associated with aluminous green spl at grain boundaries have pyrope contents ranging from 8 to 18 mol %, spessartine from 3·5 to 4%, almandine from 31 to 40% and grossular from 34 to 45% (Supplementary Data Electronic Appendix 2). In contrast, garnets overgrowing plag in some hbl-gabbros and tonalites are almandine–grossular in composition (75 and 25 mol %, respectively) with REE patterns peaking at Eu and decreasing towards La and Lu,

Table 7: Representative major and trace element analyses of amphibole from Pipe 2

	Pyroxenite						Impreg. pxt	
Sample:	P42		P47		P62		P39	Rims olivine
	Av.	2σ	Av.	2σ	Av.	2σ	Av.	2σ
Major elements (wt %)	$n=20$		$n=13$		$n=23$		$n=23$	
SiO_2	45·25	1·60	47·83	2·09	47·93	1·44	47·45	1·90
TiO_2	0·35	0·19	0·52	0·12	0·38	0·19	0·18	0·24
Cr_2O_3	0·26	0·25	0·67	0·18	0·39	0·28	0·01	0·02
Al_2O_3	12·34	0·90	9·89	1·90	10·84	1·43	12·16	1·80
FeO	6·87	2·37	5·85	0·55	5·90	0·43	7·37	2·65
MnO	0·09	0·02	0·09	0·02	0·09	0·02	0·11	0·02
NiO	0·02	0·02	0·02	0·01	0·03	0·02	0·01	0·01
MgO	16·77	1·52	17·98	1·01	17·41	0·62	16·75	1·85
CaO	12·70	0·17	12·66	0·14	12·82	0·15	12·37	0·25
Na_2O	1·48	0·13	1·09	0·23	1·00	0·23	1·25	0·26
K_2O	0·12	0·27	0·02	0·02	0·01	0·02	0·04	0·05
Total	96·25	0·52	96·61	1·13	96·81	0·42	97·72	0·36
X_{Mg}	0·90	0·07	0·90	0·02	0·89	0·01	0·84	0·08
NaK (A)	0·44	0·08	0·30	0·07	0·28	0·07	0·35	0·08
Trace elements (μg g^{-1})	$n=3$		$n=4$		$n=5$		$n=6$	
B	4·8	0·5	5·0	1·0	1·8	1/5	1·5	0·6
Sc	143·3	7·4	158·2	20·5	143·8	12·1	120·5	22·4
V	596·5	95·6	639·5	115·7	484·8	58·0	405·4	108·5
Cr	4054·3	286·8	5052·2	1508·4	3319·7	390·4	1618·2	761·6
Mn	665·7	29·4	683·1	47·2	613·9	59·9	742·2	144·6
Co	56·6	2·0	58·2	11·1	47·0	3·2	52·4	3·7
Ni	245·1	12·5	230·3	48·2	233·5	15·8	208·4	19·0
Cu	12·6	5·8	2·5	2·0	3·5	5·9	0·3	0·3
Zn	23·3	4·3	20·7	6·5	12·8	2·5	20·8	3·5
Li	1·68	0·36	0·89	0·30	2·32	0·65	0·56	0·20
Mo	<0·04		<0·1		<0·06		<0·065	
Cs	0·104	0·008	0·156	0·160	0·044	0·006	0·052	0·014
Rb	4·39	1·57	29·54	44·48	1·40	0·35	2·98	1·27
Ba	19·94	3·36	26·38	24·32	6·88	1·36	7·73	3·13
Th	0·0107	0·0026	0·0082	0·0022	0·0184	0·0011	0·0305	0·0091
U	0·0067	0·0015	0·0047	0·0014	0·0098	0·0062	0·0145	0·0019
Nb	0·2230	0·0726	0·5105	0·5263	0·0959	0·0102	0·1911	0·0563
Ta	0·0094	0·0018	0·0200	0·0177	0·0057	0·0031	0·0127	0·0058
La	0·171	0·004	0·203	0·041	0·135	0·007	0·264	0·037
Ce	0·627	0·024	0·750	0·117	0·508	0·029	1·108	0·103
Pb	1·166	0·192	0·532	0·226	1·169	0·116	0·257	0·051
Pr	0·134	0·006	0·166	0·025	0·114	0·003	0·239	0·027
Sr	47·12	1·04	37·95	11·51	49·71	6·38	40·54	11·24
Nd	1·04	0·01	1·18	0·16	0·92	0·03	1·74	0·31
Sm	0·688	0·008	0·668	0·045	0·611	0·062	0·957	0·220
Zr	2·45	0·28	3·39	0·76	1·56	0·07	8·04	1·16
Hf	0·128	0·023	0·162	0·028	0·078	0·018	0·384	0·132
Eu	0·402	0·020	0·391	0·052	0·377	0·025	0·475	0·114
Gd	1·37	0·10	1·36	0·17	1·26	0·08	1·67	0·40
Tb	0·266	0·016	0·266	0·026	0·257	0·020	0·315	0·071
Dy	2·13	0·15	2·04	0·21	1·93	0·12	2·31	0·50
Y	12·04	1·10	11·78	1·52	10·97	0·75	12·59	2·61
Ho	0·477	0·056	0·467	0·043	0·453	0·011	0·504	0·100
Er	1·39	0·09	1·44	0·20	1·33	0·07	1·47	0·27
Ti	4561	1214	4862	1249	3342	328	5271	1674
Tm	0·212	0·019	0·201	0·027	0·212	0·016	0·213	0·042
Yb	1·40	0·15	1·41	0·23	1·43	0·12	1·44	0·24
Lu	0·212	0·025	0·211	0·027	0·226	0·010	0·225	0·035

(continued)

Table 7: Continued

Sample:	Impreg. pxt P52	Symplectite	Pyroxenite P68host		Hbl-gabbro P68vein		Hbl tonalite P98	
	Av.	2σ	Av.	2σ	Av.	2σ	Av.	2σ
Major elements (wt %)	$n=6$		$n=10$		$n=20$		$n=15$	
SiO_2	47·72	2·96	46·92	1·21	44·70	2·25	44·01	2·11
TiO_2	0·12	0·14	0·59	0·47	0·51	0·19	0·96	0·49
Cr_2O_3	0·04	0·06	0·45	0·27	0·00	0·00	0·00	0·01
Al_2O_3	12·21	2·90	10·79	0·96	11·94	1·96	12·08	3·17
FeO	5·68	0·36	7·56	2·14	17·19	4·51	19·22	1·23
MnO	0·08	0·02	0·15	0·08	0·23	0·12	0·41	0·04
NiO	0·02	0·02	0·03	0·02	0·01	0·01	0·01	0·01
MgO	17·47	1·18	17·04	1·33	10·50	3·30	8·60	2·10
CaO	12·68	0·18	12·42	0·40	11·60	0·64	10·93	0·41
Na_2O	1·09	0·25	1·54	0·20	1·27	0·15	1·78	0·15
K_2O	0·05	0·05	0·01	0·01	0·03	0·01	0·05	0·10
Total	97·18	0·56	97·49	0·34	97·98	0·52	98·05	0·40
X_{Mg}	0·89	0·01	0·85	0·06	0·55	0·15	0·44	0·08
NaK (A)	0·31	0·08	0·42	0·05	0·37	0·05	0·53	0·06
Trace elements (μg g^{-1})	$n=4$		$n=1$		$n=2$		$n=2$	
B	2·8	0·0	4·0		3·7	0·2	4·0	1·5
Sc	101·1	11·6	126·6		63·9	36·5	84·5	1·6
V	237·0	31·6	436·2		194·7	76·9	20·2	1·2
Cr	901·7	379·8	2453·9		1543·4	1538·0	0·3	0·1
Mn	809·8	51·7	699·5		1514·8	274·5	3018·9	76·6
Co	52·9	1·8	56·8		56·3	5·4	41·1	0·2
Ni	217·3	6·1	279·0		177·1	93·1	6·2	2·3
Cu	1·0	1·1	13·9		42·7	49·3	5·0	7·0
Zn	16·1	2·1	18·9		72·3	49·2	174·2	8·1
Li	2·39	0·18	1·31		0·88	0·05	2·54	0·31
Mo	0·033	0·012	0·062		0·049	1/2	<0·01	
Cs	0·045	0·015	0·028		0·007	1/2	0·076	0·064
Rb	1·94	0·75	0·26		0·13	0·03	0·12	0·08
Ba	10·30	0·54	4·06		0·74	0·22	1·89	0·79
Th	0·0617	0·0116	0·0047		0·0007	0·0002	0·0013	0·0002
U	0·0226	0·0034	0·0028		0·0005	1/2	0·0007	1/2
Nb	0·2510	0·0961	0·0679		0·1544	0·0270	0·2828	0·0555
Ta	0·0056	0·0017	0·0028		0·0064	0·0044	0·0088	0·0032
La	0·228	0·015	0·128		0·446	0·092	0·422	0·008
Ce	0·912	0·075	0·532		2·072	0·446	2·675	0·158
Pb	0·225	0·093	1·161		0·043	0·004	0·082	0·002
Pr	0·178	0·016	0·122		0·469	0·107	0·771	0·054
Sr	20·11	0·75	43·71		8·62	0·02	12·23	0·21
Nd	1·16	0·17	1·00		3·31	0·91	6·80	0·49
Sm	0·482	0·083	0·639		1·483	0·550	4·310	0·339
Zr	3·55	0·87	1·52		4·79	2·04	13·48	0·28
Hf	0·138	0·044	0·099		0·265	0·230	0·581	0·045
Eu	0·360	0·027	0·356		1·484	0·452	2·006	0·073
Gd	0·76	0·16	1·29		2·14	0·71	7·95	0·57
Tb	0·144	0·031	0·272		0·369	0·094	1·508	0·095
Dy	1·04	0·23	2·01		2·67	0·78	11·41	0·81
Y	6·12	1·53	11·19		13·44	3·19	58·68	3·97
Ho	0·244	0·058	0·452		0·558	0·136	2·485	0·154
Er	0·74	0·19	1·37		1·54	0·32	7·06	0·46
Ti	2436	366	2656		2114	325	6420	237
Tm	0·124	0·031	0·194		0·213	0·038	0·986	0·037
Yb	0·92	0·19	1·37		1·41	0·05	6·33	0·18
Lu	0·159	0·029	0·191		0·192	0·004	0·894	0·028

(continued)

Table 7: Continued

Sample:	Hbl tonalite P63		Hbl-gabbronorite P67	
	Av.	2σ	Av.	2σ
Major elements (wt %)	$n=15$		$n=24$	
SiO_2	46·99	0·84	44·62	0·98
TiO_2	0·65	0·11	0·70	0·18
Cr_2O_3	0·01	0·01	0·35	0·22
Al_2O_3	9·85	0·69	12·23	1·30
FeO	14·77	0·38	9·16	0·99
MnO	0·37	0·06	0·12	0·02
NiO	0·00	0·00	0·02	0·02
MgO	12·76	0·54	15·14	0·83
CaO	11·44	0·43	12·32	0·69
Na_2O	2·01	0·27	2·32	0·28
K_2O	0·10	0·04	0·04	0·05
Total	98·95	0·52	97·03	0·41
X_{Mg}	0·61	0·02	0·77	0·04
NaK (A)	0·59	0·08	0·66	0·08
Trace elements (μg g^{-1})	$n=2$		$n=4$	
B	5·2	0·3	1·4	1/4
Sc	33·4	0·9	106·2	17·0
V	744·9	328·7	412·2	100·8
Cr	1·9	0·0	837·8	314·9
Mn	2824·3	200·8	886·4	62·9
Co	58·2	0·1	66·6	2·1
Ni	78·8	6·6	174·3	10·0
Cu	1·7	0·1	4·4	8·7
Zn	90·0	1·6	28·8	6·9
Li	6·11	1·65	0·63	0·14
Mo	<0·01		<0·06	
Cs	0·065	0·039	0·083	0·095
Rb	0·31	0·01	1·49	0·21
Ba	2·84	1·19	5·70	0·54
Th	0·0028	0·0003	0·0157	0·0019
U	0·0009	0·0003	0·0070	0·0019
Nb	0·2133	0·0728	0·1995	0·0461
Ta	0·0063	0·0021	0·0083	0·0028
La	0·925	0·110	0·275	0·019
Ce	4·510	0·707	1·274	0·070
Pb	0·184	0·003	0·272	0·125
Pr	1·100	0·225	0·279	0·016
Sr	7·74	0·33	33·84	4·80
Nd	8·43	1·94	2·05	0·08
Sm	4·005	0·969	1·116	0·070
Zr	13·24	3·28	4·31	0·12
Hf	0·674	0·117	0·201	0·022
Eu	2·186	0·395	0·610	0·045
Gd	6·54	1·24	2·01	0·19
Tb	1·197	0·220	0·385	0·049
Dy	8·75	1·80	2·83	0·36
Y	50·05	11·18	15·72	1·94
Ho	1·989	0·412	0·620	0·084
Er	5·98	1·25	1·80	0·22
Ti	4764	591	4762	940
Tm	0·932	0·227	0·269	0·041
Yb	6·60	1·69	1·84	0·28
Lu	1·042	0·272	0·271	0·042

indicating a non-magmatic origin (SD Electronic Appendix 2).

Plagioclase (Table 9) invading grain boundaries within the infiltrated pyroxenites has the highest X_{An} of 0·96–0·99. As to be expected, with increasing degree of fractionation, X_{An} decreases steadily from the hbl-gabbronorite (0·89–0·97) to the hbl-gabbro dyke margins (0·76–0·94) to the inner part of the hbl-gabbro dykes (0·40–0·60) and to the tonalites (0·15–0·77). K_2O is always below detection limit. The concentrations of REE and the size of the Eu anomaly increase with decreasing An content (Fig. 14).

Epidote is found in the most differentiated rocks (i.e. in the tonalite dykes). Those that have a clear magmatic habit have X_{ep} ranging from 0·33 to 0·48, and MnO from 0·15 to 0·44 wt % (SD Electronic Appendix 2).

DISCUSSION

The constituent minerals of Pipe 1 and Pipe 2 show continuous and complementary evolutionary trends reflecting the differentiation of a common parental melt. This interpretation allows reconstruction of the differentiation of the percolating melt. Modeling melt evolution in such open systems can only barely constrain the melt percolation because of the unknown melt/cumulate ratios during melt circulation. We thus qualify the cumulative sequence based on mineral compositions only and discuss, using experimental constraints, the liquid evolution in terms of major elements (Fig. 15). We discuss these results in combination with the mantle sequence underlying the Sapat crust and finally compare the calculated seismic P-wave velocities with geophysical observations made in modern magmatic arcs.

Differentiation sequence

The primitive parental melt initially crystallized ol, spl and cpx leading to the formation of the dunites and clinopyroxenites of Pipe 1. Very little chemical evolution is seen in these cumulates and the range of compositions is best explained by the liquid being either cpx- or ol-saturated, and by re-equilibration during melt percolation and melt–rock reaction as shown by the textural relationships. A rather limited amount of differentiation is sufficient to explain the concomitant decrease of X_{Mg} in cpx and ol in the ol-clinopyroxenites, whereas Al_2O_3 and TiO_2 in cpx increase. Hbl is a late crystallizing phase in most clinopyroxenites and in peritectic relationship with cpx, where cpx reacts with the percolating melt to produce hbl (cpx + melt = hbl) (Foden & Green, 1992; Gillis & Meyer, 2001). Cpx in equilibrium with hbl and the hbl itself have major element and REE concentrations in the upper range of those observed for this limited amount of differentiation. Pipe 1 and Pipe 2 show the same textural relationships between hbl and cpx, the same peritectic reaction, as well as a compostional overlap of the most evolved minerals of Pipe 1 with the least evolved minerals found in Pipe 2, hence forming a single magmatic suite. Similarly, Pipe 2 hbl and cpx in wehrlite have the same trace element concentrations as those of Pipe 1 hbl and cpx. The crystallization of hbl induces an enrichment of Si, Na, and Ti in the rising residual melt. Concomitantly, ol reacts peritectically with the increasingly Si-rich melt yielding aluminous low-Ti opx. With increasing differentiation, hbl becomes more

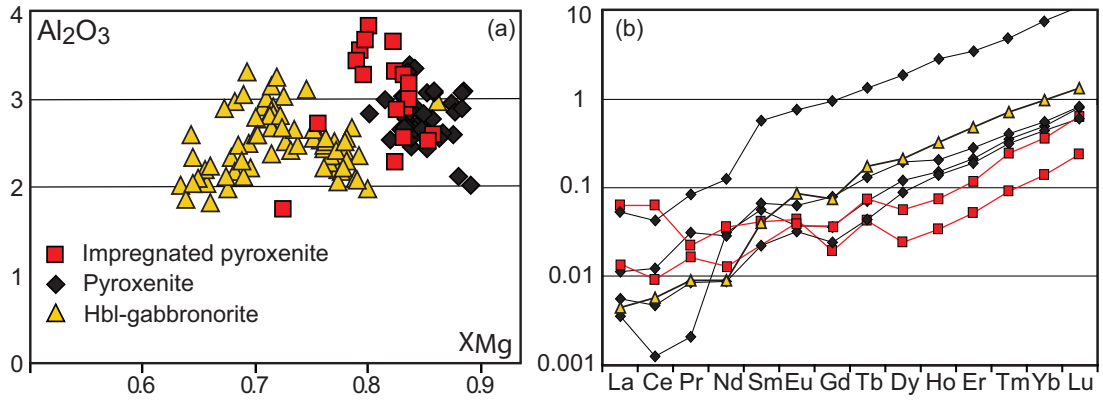

Fig. 13. Opx compositions from Pipe 2. (a) X_{Mg} vs Al_2O_3 (b) Chondrite-normalized REE patterns. The highest REE contents are in peritectic opx (sample P62).

Na- and Ti-rich, reflecting enrichment of these elements in the melt. These peritectic reactions are most prominent in the fully reacted pyroxenites in which hbl + opx + plag ± hercynitic spl crystallized from the invading melt. In these former pyroxenites, magmatic hbl and opx still coat ol, whereas cpx is completely consumed and plag occurs for the first time in the crystallization sequence. In these infiltrated pyroxenites, the major element composition of hbl is similar to that in the non-plag-bearing pyroxenites although its trace element concentrations are higher (Figs 11 and 12). Higher REE and lower Sr concentrations mark the appearance of plag. The Hbl-gabbronorite marks the co-crystallization of opx + hbl + cpx in a granophyric texture and interstitial plag marks further differentiation of the cooling melt. Cpx and hbl in the hbl-gabbronorites are more evolved, have lower X_{Mg}, higher Al_2O_3, TiO_2 and Na_2O than those from pyroxenites (Figs 9 and 11), and have increased trace element concentrations. The fractionation of anorthite-rich plag leads to a continued increase in melt SiO_2 content. The strong decrease of Ti, Pb and Sr in hbl from the tonalite suggests fractionation of an (Fe–)Ti-oxide phase and plag during this stage. Edenite in the leucocratic patches and tonalites represents the most evolved magmatic amphibole in both Pipe 1 and Pipe 2. Edenites have the lowest X_{Mg} and the highest Ti contents, but show a decrease in Na_2O with decreasing X_{Mg}. They also have the highest REE concentrations, with slightly fractionated HREE in some of the samples (e.g. P98). The disappearance of the Pb anomaly (compared with less differentiated amphiboles), the presence of Ti and Sr negative anomalies, and the lowest concentrations of the most incompatible elements (Cs, Rb, Ba, Th and U) in edenite indicate that these elements have become compatible in previously fractionated minerals and suggest that the percolating melts were plag-saturated upon edenite crystallization.

In summary, the main fractionation sequence is ol–sp, followed by ol + cpx, and culminating in cpx + hbl in peritectic relationship (Fig. 15). Reactions continued with the appearance of hercynite, opx and hbl replacing olivine, followed by An-rich plag. Subsequently, the liquid followed a path allowing the co-crystallization of opx + cpx + hbl and then plag that ended with crystallization of hbl, plag and Ti-oxides together and finally minute amounts of ep, bt and quartz in the most differentiated tonalites.

Pressure estimates

Magmatic epidote in the tonalites suggests pressures above 5 kbar (Schmidt & Thompson, 1996) and epidote crystallization before quartz and plag indicates 6–8 kbar. The Al-in-hornblende barometer (Schmidt, 1992) suggests tonalite crystallization between 5 and 7 kbar.

Hornblende that re-equilibrated with plag and ol (and/or opx) during the formation of hbl + hercynitic spl ± opx symplectites between plag and ol in the infiltrated pyroxenites of Pipe 2 has a positive Eu anomaly and REE patterns with a steeper HREE segment than magmatic hbl coating ol (Fig. 10). Tremolite has overgrown olivine during the late, cooler stage of symplectite formation (Ikeda *et al.*, 2007). Conventional thermobarometry (e.g. Fe–Mg exchange) and pseudosection analysis of similar symplectites place their formation in granulite-facies conditions near a pressure of 7 kbar in the presence of deuteric fluids (Ballhaus & Berry, 1991; Claeson, 1998; de Haas *et al.*, 2002; Ikeda *et al.*, 2007; Cruciani *et al.*, 2008; Helmy *et al.*, 2008). We thus deduce that the symplectites formed during isobaric cooling at ~7 kbar and ultimately equilibrated in a fluid-rich environment.

Magmatic garnet is not ubiquitous but is present with hercynite at grain boundaries of the Pipe 2 pyroxenites that show extensive reactional textures. This garnet may indicate that the magmatic system formed at pressure near the super-solidus stability of garnet, which is >9 kbar if $P_{H2O} < P_{tot}$ (Green & Ringwood, 1968). As argued below, it is most likely that $P_{H2O} \approx P_{tot}$ at the stage of hercynite crystallization, indicating pressures near 8 kbar, consistent with those obtained for the crystallization of an interlayered tonalitic sill in the host metaplutonic rocks (Bouilhol, 2008). Taking into account these constraints, the studied pipes at Sapat were

Table 8: Representative major and trace element analyses of orthopyroxene from Pipe 2

Sample:	Pyroxenite						Impreg. pxt			
	P42		P47		P68host		P52	Rims ol.	P39	
	Av.	2σ	Av.	2σ	Av.	2σ	Av.	2σ	Av.	2σ
Major elements (wt %)										
	$n = 25$		$n = 10$		$n = 3$		$n = 4$		$n = 18$	
SiO_2	54·15	0·96	53·80	1·08	53·56	0·16	55·07	0·13	54·31	0·66
TiO_2	0·06	0·02	0·08	0·06	0·05	0·00	0·11	0·01	0·04	0·02
Cr_2O_3	0·14	0·06	0·21	0·08	0·18	0·04	0·15	0·01	0·01	0·02
Al_2O_3	2·67	0·21	2·83	0·55	3·37	0·01	2·51	0·09	2·87	0·81
FeO	11·91	0·44	11·29	2·51	12·58	0·11	10·88	0·08	13·95	1·58
MnO	0·27	0·02	0·27	0·05	0·30	0·02	0·26	0·02	0·33	0·05
NiO	0·00	0·01	0·02	0·02	0·03	0·01	0·02	0·02	0·02	0·01
MgO	30·43	0·38	28·59	4·63	29·66	0·01	31·16	0·02	29·21	1·34
CaO	0·49	0·11	2·81	7·47	0·60	0·01	0·54	0·04	0·38	0·12
Na_2O	0·01	0·01	0·01	0·02	0·00	0·00	0·00	0·00	0·00	0·01
Total	100·15	0·97	99·92	0·58	100·31	0·22	100·69	0·05	101·12	0·31
X_{Mg}	0·85	0·02	0·85	0·03	0·83	0·00	0·85	0·56	0·81	0·03
Trace elements (μg g^{-1})										
	$n = 3$		$n = 2$		$n = 3$		$n = 4$		$n = 2$	
B	2·6	0·1	2·5	0·1	1·9	0·2	2·2	0·3	0·7	0·1
Sc	38·1	4·3	38·7	8·3	38·3	0·5	21·1	2·3	31·8	0·0
V	133·9	14·1	119·7	40·2	132·1	1·8	48·9	4·6	77·2	1·9
Cr	1182·2	63·6	1343·1	478·4	2069·6	171·5	124·3	30·4	249·0	18·2
Mn	2099·1	32·2	2022·5	111·8	1980·3	42·2	1970·1	25·9	2269·6	22·9
Co	79·5	0·7	82·4	9·4	79·1	1·9	74·6	1·3	77·5	1·5
Ni	152·4	3·0	165·1	17·8	179·5	3·4	142·4	2·4	138·3	5·6
Cu	29·0	24·2	9·7	13·0	30·8	48·9	0·1	0·1	b.d.	
Zn	71·2	0·1	70·3	7·8	59·6	4·7	52·4	4·0	59·9	1·2
Li	0·3	0·1	0·2	0·1	0·2	0·0	0·7	0·3	0·2	0·1
Mo	0·011	1/3	<0·01		<0·01		0·020	0·014	0·027	1/3
Cs	0·010	0·002	0·011	0·012	0·004	0·001	0·017	0·008	0·024	0·014
Rb	0·019	0·005	0·019	0·000	0·011	0·012	0·027	0·009	0·029	0·002
Ba	0·034	0·006	0·106	0·031	0·077	0·102	0·170	0·077	0·028	0·015
Th	0·0038	0·0053	0·0009	0·0011	0·0007	0·0005	0·0056	0·0018	0·0023	0·0011
U	0·0004	0·0001	0·0002	0·0001	0·0001	0·0001	0·0232	0·0412	0·0019	0·0020
Nb	0·0011	0·0007	0·0011	0·0002	0·0012	0·0000	0·0029	0·0022	0·0019	1/2
Ta	0·0005	1/3	0·0002	1/2	0·0006	1/3	0·0005	0·0001	0·0073	0·0016
La	0·0152	0·0203	0·0027	0·0026	0·0013	0·0014	0·0148	0·0160	0·0033	1/2
Ce	0·0008	0·0003	0·0076	0·0080	0·0029	0·0024	0·0380	0·0700	0·0056	0·0058
Pb	0·0626	0·0676	0·7812	0·9261	0·0089	0·0055	0·0257	0·0146	0·0233	0·0064
Pr	0·0640	0·0902	0·0029	0·0036	0·0008	0·0006	0·0021	0·0017	0·0016	0·0016
Sr	0·098	0·014	0·246	0·177	0·092	0·133	0·906	1·388	0·133	0·082
Nd	0·0147	0·0180	0·0135	0·0108	0·0041	0·0041	0·0169	0·0269	0·0061	1/2
Sm	0·0085	0·0062	0·0103	0·0100	0·0034	0·0013	0·0063	0·0055	<0·005	
Zr	0·0854	0·0193	0·1076	0·0646	0·0491	0·0049	0·1267	0·0580	0·1731	0·0967
Hf	0·0059	0·0012	0·0062	0·0021	0·0036	0·0018	0·0041	0·0020	0·0111	0·0011
Eu	0·0022	0·0003	0·0037	0·0022	0·0019	0·0014	0·0025	0·0029	0·0022	0·0007
Gd	0·0076	0·0025	0·0164	0·0109	0·0050	0·0002	0·0040	0·0034	0·0073	0·0016
Tb	0·0026	0·0010	0·0049	0·0021	0·0016	0·0002	0·0016	0·0019	0·0028	1/2
Dy	0·0309	0·0149	0·0493	0·0181	0·0221	0·0031	0·0061	0·0035	0·0143	0·0103
Y	0·22	0·07	0·30	0·02	0·19	0·03	0·05	0·02	0·11	0·04
Ho	0·0085	0·0040	0·0116	0·0016	0·0078	0·0016	0·0019	0·0009	0·0042	0·0010
Er	0·0347	0·0111	0·0461	0·0081	0·0312	0·0052	0·0086	0·0031	0·0193	0·0110
Ti	394·7	78·2	367·2	86·3	310·8	48·7	188·4	12·9	373·6	4·3
Tm	0·009	0·002	0·010	0·001	0·008	0·000	0·002	0·001	0·006	0·002
Yb	0·083	0·017	0·092	0·012	0·074	0·009	0·024	0·010	0·062	0·007
Lu	0·020	0·004	0·021	0·000	0·015	0·001	0·006	0·002	0·016	0·001

Table 8: Continued

Sample:	P62	Pxt–peritectic	Hbl-gabbronorite P67	
	Av.	2σ	Av.	2σ
Major elements (wt %)	$n=3$		$n=39$	
SiO_2	54·95	1·64	53·52	0·80
TiO_2	0·05	0·01	0·07	0·02
Cr_2O_3	0·16	0·16	0·16	0·04
Al_2O_3	1·97	1·24	2·49	0·29
FeO	12·72	1·62	16·33	1·60
MnO	0·32	0·03	0·37	0·03
NiO	0·03	0·01	0·02	0·01
MgO	29·77	1·84	26·61	1·47
CaO	0·35	0·14	0·57	0·17
Na_2O	0·00	0·00	0·00	0·01
Total	100·32	0·26	100·14	0·57
X_{Mg}	0·82	0·02	0·75	0·03
Trace elements (μg g^{-1})	$n=3$		$n=3$	
B	4·5	0·9	0·6	0·1
Sc	556·6	45·7	40·4	6·8
V	1626·3	144·4	131·6	23·4
Cr	14661·2	1804·8	515·8	191·6
Mn	24700·2	487·4	2755·6	72·2
Co	831·4	16·1	98·3	1·5
Ni	1607·3	17·2	110·3	16·2
Cu	14·9	1·3	7·6	6·8
Zn	604·6	39·4	116·5	10·8
Li	3·1	0·7	0·3	0·0
Mo	<0·022		<0·023	
Cs	0·118	0·045	0·068	0·056
Rb	0·330	0·158	0·037	0·039
Ba	0·983	0·781	0·103	0·060
Th	0·0026	0·0022	0·0004	0·0002
U	0·0228	0·0183	0·0004	0·0003
Nb	0·0167	0·0061	0·0013	1/3
Ta	0·0102	1/3	<0·001	
La	0·0125	0·0067	0·0011	0·0003
Ce	0·0257	0·0080	0·0035	0·0014
Pb	0·1570	0·0942	0·1854	0·1744
Pr	0·0079	0·0022	0·0009	0·0007
Sr	1·705	0·790	0·146	0·084
Nd	0·0570	0·0170	0·0042	0·0014
Sm	0·0863	0·0471	0·0061	1/3
Zr	1·0350	0·0942	0·1447	0·0128
Hf	0·0570	0·0106	0·0083	0·0027
Eu	0·0430	0·0076	0·0050	0·0016
Gd	0·1903	0·0784	0·0154	0·0046
Tb	0·0490	0·0063	0·0065	0·0021
Dy	0·4723	0·0447	0·0535	0·0132
Y	3·87	0·13	0·48	0·14
Ho	0·1593	0·0115	0·0185	0·0064
Er	0·5657	0·0372	0·0789	0·0215
Ti	4103	218	555	142
Tm	0·122	0·015	0·018	0·006
Yb	1·283	0·132	0·165	0·050
Lu	0·274	0·036	0·034	0·009

emplaced at pressures of ~7–8 kbar in the lower crust of the Kohistan Arc.

Experimental constraints on parental melt, liquid line of descent and water content

Differentiation starts with extensive ol + spl fractionation followed by cpx and then hbl; opx and plag are absent from the early cumulates. Experiments on the differentiation and liquid lines of descent of mantle-derived basalts and picrite demonstrate the influence of water on the appearance of liquidus minerals (Kaegi, 2000; Muntener *et al.*, 2001; Pichavant *et al.*, 2002*a*, 2002*b*; Grove *et al.*, 2003; Prouteau & Scaillet, 2003; Feig *et al.*, 2006; Muntener & Ulmer, 2006; Pichavant & Macdonald, 2007; Alonso-Perez *et al.*, 2009; Nandedkar *et al.*, 2014; Melekhova *et al.*, 2015). Increasing water content and decreasing pressure suppress opx and plag stability and extend the temperature interval of ol, spl and cpx fractionation, while stabilizing hbl. Increasing pressure under hydrous conditions, or increasing silica content of the parental primary melt, would increase the stability of opx during the early stages of differentiation, leading to (ol-)websterites, and ultimately stabilizing garnet and amphibole (at $T \leq 1070^\circ$C). Increasing oxygen fugacity has the same effect as increasing water content. Nandedkar *et al.* (2014) studied fractional crystallization at 7 kbar and showed that for a starting water content of about 3·5 wt % plag appears at the liquidus just before hbl at 1040°C, which is not observed here. In contrast, for parental basaltic liquids with water contents between 5 and 8 wt %, cpx and ol fractionate extensively before hbl appears in a peritectic relationship with cpx and melt at ~1050°C, as observed in Pipe 1. These amphibole-saturated melts become fluid saturated at ~1000°C at about 8 wt % H_2O (e.g. Foden & Green, 1992; Kaegi, 2000). The geodes filled with fluid-derived minerals in the same pipe reflect the H_2O saturation of the melt at least at the end of the hbl crystallization stage. Furthermore, prograde olivine is overgrowing serpentine (Fig. 6d) and ubiquitous calcite (Figs 6 and 7). This prograde decomposition of serpentine probably results from magmatic heat. In this case, serpentine would form while there was still magma flow, thus indicating that early serpentinization resulted from magmatic fluids exsolved in the early stages of pipe formation. The early stage cumulate succession identified in Pipe 1 is thus consistent with experiments on fractional crystallization of a parental basaltic composition that contained ≥5 wt % H_2O and that reached fluid-saturation while the melt was still basaltic (Fig. 15). The cpx–hbl peritectic relationship is also found in the most primitive cumulates of Pipe 2, followed by the appearance of opx and hbl at the expense of ol. The peritectic formation of amphibole at the expense of cpx increases the silica content of the remaining liquid (Cawthorn, 1976; Cawthorn & O'Hara, 1976; Foden & Green, 1992); however, in an open system such as the magma conduits investigated here, it is unclear to what extent (Fig. 15).

The crystallization sequences in calc-alkaline magmas are complex and may depend on subtle differences in the bulk compositions of the parental melt, on pressure and on the melt's H_2O content. The peritectic reaction boundary consuming cpx and crystallizing amphibole was investigated by Foden & Green (1992). This reaction leads towards high-Al basalt

Table 9: Representative major and trace element analyses of plagioclase from Pipe 2

	Impregn. pxt				Hbl gabbro		Hbl-gabbronorite		Tonalite			
Sample:	P52		P39		P68		P67		P98		P63	
	Av.	2σ	Av.	2σ	Av.	2σ	Av.	2σ	Av.	2σ	Av.	2σ
Major elements (wt %)												
	n = 34		*n* = 12		*n* = 49		*n* = 12		*n* = 59		*n* = 17	
SiO_2	43·36	0·42	43·39	0·27	53·21	6·03	44·45	0·39	53·63	2·88	63·20	3·96
Al_2O_3	35·48	0·41	35·68	0·36	30·96	3·56	34·51	0·41	28·77	1·71	23·61	2·31
FeO	0·11	0·04	0·19	0·16	0·15	0·11	0·14	0·04	0·11	0·15	0·08	0·06
MgO	0·02	0·01	0·00	0·00	0·03	0·14	0·00	0·00	0·01	0·03	0·00	0·00
CaO	19·69	0·26	20·01	0·24	11·70	4·50	19·10	0·28	12·69	2·26	4·58	3·02
Na_2O	0·29	0·12	0·18	0·13	4·41	2·29	0·74	0·10	4·36	1·18	8·57	1·56
K_2O	0·02	0·01	0·00	0·00	0·02	0·03	0·00	0·00	0·01	0·01	0·02	0·01
Total	99·02	0·76	99·49	0·33	100·52	1·22	98·97	0·57	99·59	0·82	100·07	0·49
An	0·97	0·01	0·98	0·01	0·59	0·22	0·93	0·01	0·62	0·11	0·23	0·15
Ab	0·03	0·01	0·02	0·01	0·41	0·22	0·07	0·01	0·38	0·11	0·77	0·15
Or	0·00	0·00	0·00	0·00	0·00	0·00	0·00	0·00	0·00	0·00	0·00	0·00
Trace elements (μg g^{-1})												
	n = 11		*n* = 3		*n* = 3		*n* = 3		*n* = 4		*n* = 3	
B	4·76	0·31	0·29	1/3	3·53	0·36	0·86	0·63	4·99	1·35	5·13	0·34
Sc	0·39	0·12	0·04	0·01	0·35	0·06	0·11	0·01	0·31	0·05	0·44	0·02
V	0·50	0·99	0·02	0·01	0·05	0·05	0·23	0·11	0·05	0·03	0·05	1/3
Cr	1·35	1·73	0·20	0·10	0·32	0·09	0·82	0·84	0·30	0·05	0·29	0·05
Mn	21·6	4·7	7·5	1·1	13·2	3·3	128·3	218·8	23·9	5·4	9·2	8·6
Co	0·24	0·25	0·04	0·02	0·11	0·06	3·59	6·95	0·05	0·02	0·04	0·04
Ni	3·89	2·49	<1		3·96	1/3	38·95	1/3	2·10	1/4	<0·9	
Cu	0·09	0·04	0·02	1/3	33·35	28·46	47·17	1/3	16·92	15·18	0·49	0·26
Zn	0·50	0·26	0·19	0·15	2·89	0·42	5·83	10·01	1·87	0·84	0·99	0·26
Li	1·00	0·55	0·09	1/3	0·54	0·37	1·95	2·62	0·59	0·26	0·65	0·33
Mo	0·03	0·01	<0·02		<0·02		<0·04		0·02	1/4	0·02	1/3
Cs	0·029	0·015	0·007	0·003	0·023	0·012	0·091	0·140	0·027	0·023	0·029	0·029
Rb	0·053	0·051	0·011	0·002	0·102	0·041	0·130	0·193	0·105	0·169	0·079	0·068
Ba	3·95	0·78	0·94	0·39	4·08	0·68	5·48	7·24	6·37	1·99	32·72	6·74
Th	0·0156	0·0224	0·0001	0·0000	0·0002	1/3	0·0007	1/3	0·0001	1/4	0·0002	0·0001
U	0·0067	0·0076	<0·0002		0·0051	0·0043	0·0027	0·0036	0·0000	1/4	0·0133	0·0230
Nb	0·0024	0·0004	<0·002		0·0016	1/3	<0·002		0·0009	1/4	0·0010	
Ta	0·0021	0·0001	0·0015	0·0008	<0·0004		<0·002		0·0010	1/4	<0·0004	
La	0·061	0·018	0·017	0·005	0·240	0·026	0·083	0·011	0·318	0·017	0·334	0·126
Ce	0·063	0·041	0·021	0·009	0·516	0·077	0·131	0·031	0·578	0·028	0·379	0·161
Pb	0·553	0·141	0·097	0·009	0·470	0·091	0·791	1·021	0·656	0·060	2·573	0·304
Pr	0·005	0·005	0·001	0·001	0·066	0·011	0·013	0·004	0·066	0·005	0·032	0·015
Sr	162·9	7·6	60·3	2·8	253·8	3·5	142·3	15·2	284·4	16·9	427·5	45·4
Nd	0·0138	0·0178	0·0038	0·0017	0·2968	0·0711	0·0470	0·0184	0·2855	0·0200	0·1044	0·0640
Sm	0·0093	0·0057	0·0097	1/3	0·0589	0·0155	0·0187	1/3	0·0459	0·0036	0·0149	0·0048
Zr	0·0745	0·1293	<0·0025		<0·001		<0·005		0·0012	1/4	0·0017	0·0002
Hf	0·0043	0·0062	<0·001		<0·0006		<0·002		<0·0008		<0·0008	
Eu	0·0570	0·0078	0·0278	0·0037	0·7143	0·0709	0·1187	0·0253	0·5620	0·0660	0·3006	0·0829
Gd	0·0045	0·0012	<0·0001		0·0459	0·0172	0·0051	1/3	0·0331	0·0031	0·0087	0·0063
Tb	0·0006	0·0002	<0·0001		0·0049	0·0022	0·0012	0·0002	0·0032	0·0005	0·0019	1/3
Dy	0·0022	0·0008	<0·0001		0·0192	0·0082	0·0066	0·0061	0·0169	0·0021	0·0026	0·0027
Y	0·0056	0·0038	<0·0001		0·0644	0·0319	0·0185	0·0252	0·0627	0·0027	0·0231	0·0113
Ho	0·0007	0·0004	<0·0001		0·0023	0·0017	0·0010	0·0003	0·0024	0·0005	0·0006	0·0003
Er	0·0042	0·0051	<0·0001		0·0041	0·0019	0·0069	1/3	0·0047	0·0028	0·0010	0·0002
Ti	6·17	4·53	0·83	0·70	27·68	9·55	5·12	4·29	16·23	6·40	10·42	3·50
Tm	0·0010	0·0004	0·0007	1/3	0·0005	1/3	0·0029	0·0004	0·0006	0·0002	0·0009	0·0002
Yb	0·0037	0·0018	<0·001		0·0023	0·0020	0·0050	0·0045	0·0036	0·0029	0·0028	1/3
Lu	0·0003	<0·0002	<0·0004		0·0007	0·0001	0·0020	1/3	0·0006	0·0003	0·0005	0·0003

compositions. Equilibrium crystallization along the olivine–amphibole cotectic leads to the olivine + melt = amphibole + opx peritectic (Cawthorn & O'Hara, 1976). Instead, fractional crystallization where peritectic amphibole mantles olivine, as observed in Sapat (Fig. 7f), causes the evolving melt to leave the olivine–amphibole cotectic and evolve towards the plagioclase + amphibole cotectic. Further complications arise because the appearance of amphibole may involve a distributary point where, depending on the parental melt composition, the liquid line of descent may follow two different paths, following either a cotectic involving cpx + amphibole or a peritectic involving opx and amphibole (Ehlers, 1972; Krawczynski *et al.*, 2012)

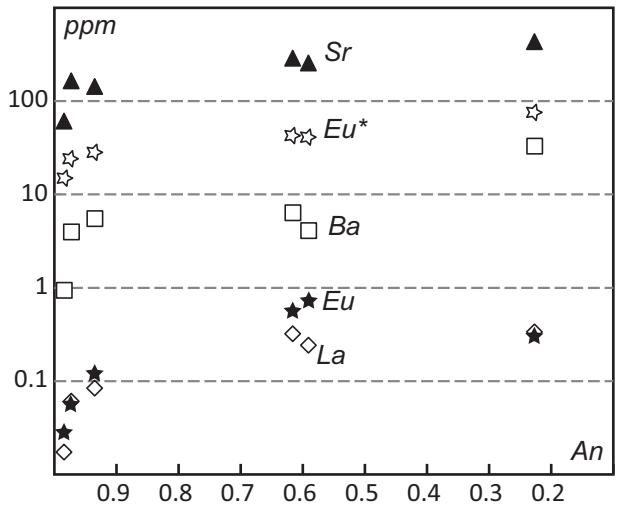

Fig. 14. Variation of Pipe 2 plag composition in key trace elements as a function of anorthite content. Eu* is Eu anomaly $= 2Eu_N/(Sm_N + Gd_N)$.

(Fig. 15). Along a reactive path, the consumption of cpx may be followed by the peritectic appearance of opx and hbl at the expense of ol.

Consequently, fractional crystallization along the olivine–amphibole peritectic may be followed by a crystallization sequence dominated by plagioclase. This sequence leads the melts to evolve towards dacitic compositions following a calc-alkaline differentiation trend that ultimately produces peraluminous granitoids (e.g. Nandedkar *et al.*, 2014). The melts that follow equilibrium crystallization of cpx, hbl and plag and that reach the distributary point most probably form gabbroic rocks. The two modes of crystallization are reflected in the two compositional trends of hbl: a trend of increasing TiO_2 and Na_2O for a small decrease in X_{Mg} (essentially hbl crystallizing before plag), and a trend where X_{Mg} decreases more rapidly for a lower increase in TiO_2 and Na_2O. This duality is also reflected in the evolution of Sr and Pb with X_{Mg}.

In Pipe 2 some magmatic features are overprinted by high-temperature re-equilibration involving a fluid phase (e.g. symplectites). This is in accordance with fluid saturation and degassing of the parental magma during its differentiation occurring, at the latest, with the completion of the amphibole-forming peritectic reactions.

Liquid lines of descent in the Kohistan lower arc crust

Two liquid lines of descent have been inferred for the Jijal and Chilas complexes (Fig. 1), both also part of the lower crust of the Kohistan arc (Jagoutz *et al.*, 2011). (1) A high-pressure hydrous liquid line of descent leading to (ol)–cpx–garnet–hbl-dominated fractionation, which generated the garnetites, garnet-hornblendites and garnet-gabbros of the Jijal complex. (2) A shallower, drier liquid line of descent, leading to (ol)–opx–cpx–plag-dominated fractionation, which generated the dominantly gabbronoritic Chilas Complex. The Jijal complex formed between *c.* 115 and 100 Ma (Burg, 2011) at 16–11 kbar (Jagoutz & Schmidt, 2012). The relatively dry magmas of the *c.* 85 Ma Chilas Complex (Schaltegger *et al.*, 2002) crystallized at 7–8 kbar and were related to intra-arc extension.

The cumulates of the Sapat pipes result from a liquid line of descent that was similarly hydrous to that of the Jijal complex, but crystallized at lower pressure. The lack of a significant garnet signature in the differentiation series of the pipes indicates that the 7–8 kbar crystallization pressure almost corresponds to the bottom of the arc crust, consistent with the presence of directly adjacent mantle (Bouilhol *et al.*, 2009, 2011*a*). The formation of the Sapat Complex at 105–99 Ma (Bouilhol *et al.*, 2011*b*) corresponds to that of the Jijal complex, indicating that in different parts of the Kohistan arc, different crustal thicknesses may have led to different contemporaneous liquid lines of descent.

Relationship between pipes and mantle

The Sapat mantle contains pyroxene-enriched zones and gabbroic lenses that resulted from melt infiltration (Bouilhol *et al.*, 2009, 2011*a*). These melt products and the crustal lithologies of the Sapat Complex have similar trace element patterns, isotopic compositions and timing of crystallization (Bouilhol *et al.*, 2011*b*). These characteristics indicate that the melts forming the olclinopyroxenite and gabbros of the crust–mantle transition zone, directly below the lower crustal sills that host the pipes, have also generated the cumulates now filling the pipes. This is indeed reflected in the observed mineral compositions, where the primitive character of the melts that sourced Pipe 1 is indicated by cumulate cpx having similar compositions to cpx in melt channels within the crust–mantle transition zone (Figs 9 and 10). The REE and slightly Al_2O_3-richer compositions of the cpx from the reacted portions of the mantle indicate reaction with the same melt that formed the pipe (Bouilhol *et al.*, 2009). In fact, ol compositions from the pipes define a differentiation trend starting from $X_{Mg} = 90$ and NiO = 0·15 wt % (Fig. 8); that is, ol compositions that are not truly primitive and that correspond to compositions at the end of the trend [decreasing NiO at almost constant X_{Mg} (Bouilhol *et al.*, 2009, 2011*a*)] observed in the ol of the mantle rocks. Following these lines of arguments, we interpret the studied pipes as magma conduits through which primitive mantle-derived melts have risen from the crust–mantle transition zone into and through the gabbroic lower crust sill complex.

Pipe emplacement

The contact between the pyroxenite pipes and the surrounding fine-grained metagabbro–hornblendite–tonalite sills is in some places sharp and in other places transitional. The sharp contacts, the absence of contact-parallel foliation in the host sills beyond 5–10 m from the contact, and the presence of enclaves of

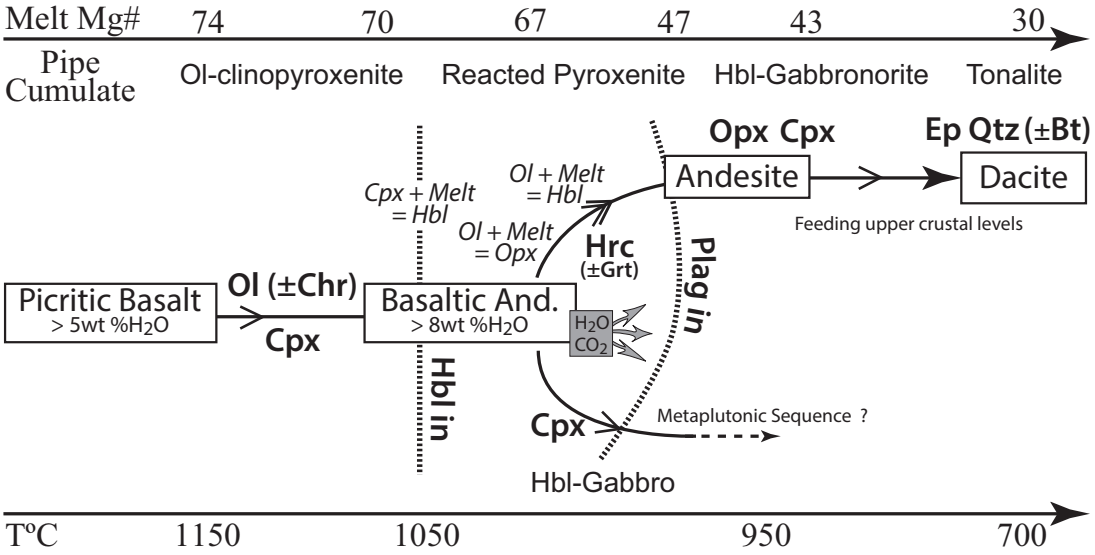

Fig. 15. Summarized differentiation sequence in the Sapat pipes in terms of liquid line of descent based on experiments. The melt Mg# has been calculated with either cpx following Wood & Blundy (1997) or hbl following Alonso-Perez *et al.* (2009). Temperatures and melt composition are estimated from the experiments cited in text.

fine-grained metagabbro within the pyroxenites demonstrate an intrusive character. The transitional contacts show that melts rising through the pipes dissolved and assimilated the fine-grained lower crustal metagabbros. The local recrystallization that visibly erased the magmatic foliation and layering of the host metagabbros in the immediate vicinity of the pipes requires heat and fluid advection from the pipes (Figs 2 and 3). We conclude that pipe emplacement involved intrusion of melt along brittle–ductile paths whose walls were consumed by thermal erosion, probably resulting in assimilation of the wall-rocks.

We contend that the present-day subvertical attitude of the pipes is not far from the original orientation. This is based on the following observations. Graded layers in the host metagabbros indicate that the present-day *c.* 40°NW dipping sequence is normal, consistent with crustal rocks lying on top of mantle rocks (Fig. 1). Undeformed, mesoscale diapirs roughly orthogonal to the layering indicate that the latter was subhorizontal at the time the pipes were intruded. We have two main possibilities. (1) The pipes have intruded still subhorizontal host sills. In this case, rotating the strike direction of the host-rocks to their original horizontal position ascribes to the pipes a pre-rotation inclination of *c.* 40°NW. (2) Alternatively, the pipes may have vertically intruded an already tilted sequence of lower crustal sills. In this case, the present-day dip of the sills is primary and represents the inclination at which the sills were emplaced to form the lower crust of the Kohistan arc. We favor the second hypothesis. Indeed, Pipe 2 in particular exposes a remarkably concentric sequence of compositional zoning with plagioclase-bearing lithologies in the middle, olivine–clinopyroxene layering along the pipe walls and pegmatitic gabbros transitional to the host gabbros at the periphery. This zoning suggests subvertical emplacement, whereas it would be inconsistent with originally strongly inclined pipes: melts principally follow vertical, gravity-controlled pressure gradients, which should give rise to asymmetry in lithological and structural arrangements of non-vertical pipes. If pegmatitic gabbros represent the last magmatic phase, their peripheral location may reflect emplacement in a decoupling interface (possibly owing to thermal contraction) between the pipes and their host-rocks.

Geophysical characteristics of the Sapat crust

High-resolution tomographic images of active arc lithosphere emphasize its heterogeneity in velocity structure with vertical, high-velocity (>7 km s^{-1}) 'columns' that rise from the seismic Moho and fade into lower- and mid-crustal material with P-wave velocities (V_p) between 6 and 7 km s^{-1} (Shillington *et al.*, 2004; Kodaira *et al.*, 2007; Takahashi *et al.*, 2008). These 'columns' have been interpreted as mafic plutons within a tonalitic to granitic crust (e.g. Kodaira *et al.*, 2007; Takahashi *et al.*, 2008). These columns are located beneath silicic volcanoes at the surface, raising the question of how and where melt is transported and differentiated. Calculated V_p values (Fig. 16) suggest that the kilometer-scale pipes mapped in the Sapat Complex can be regarded as equivalent to the geophysically imaged high-velocity columns. The Sapat pipes, essentially clinopyroxenites, are up to 10 km in diameter and have seismic velocities of ≥7·6 km s^{-1} at 7 kbar (Fig. 16). The gabbro-dominated host rocks would have a V_p of about 7 km s^{-1} at the same depth (21–25 km). These values show that the Sapat Complex would be geophysically imaged as a 7 km s^{-1} crust with kilometer-sized, near-vertical structures with $V_p > 7{\cdot}5$ km s^{-1}. This is comparable with what is reported from West Pacific active island arc systems (e.g. Izu–Bonin; Kodaira *et al.*, 2007).

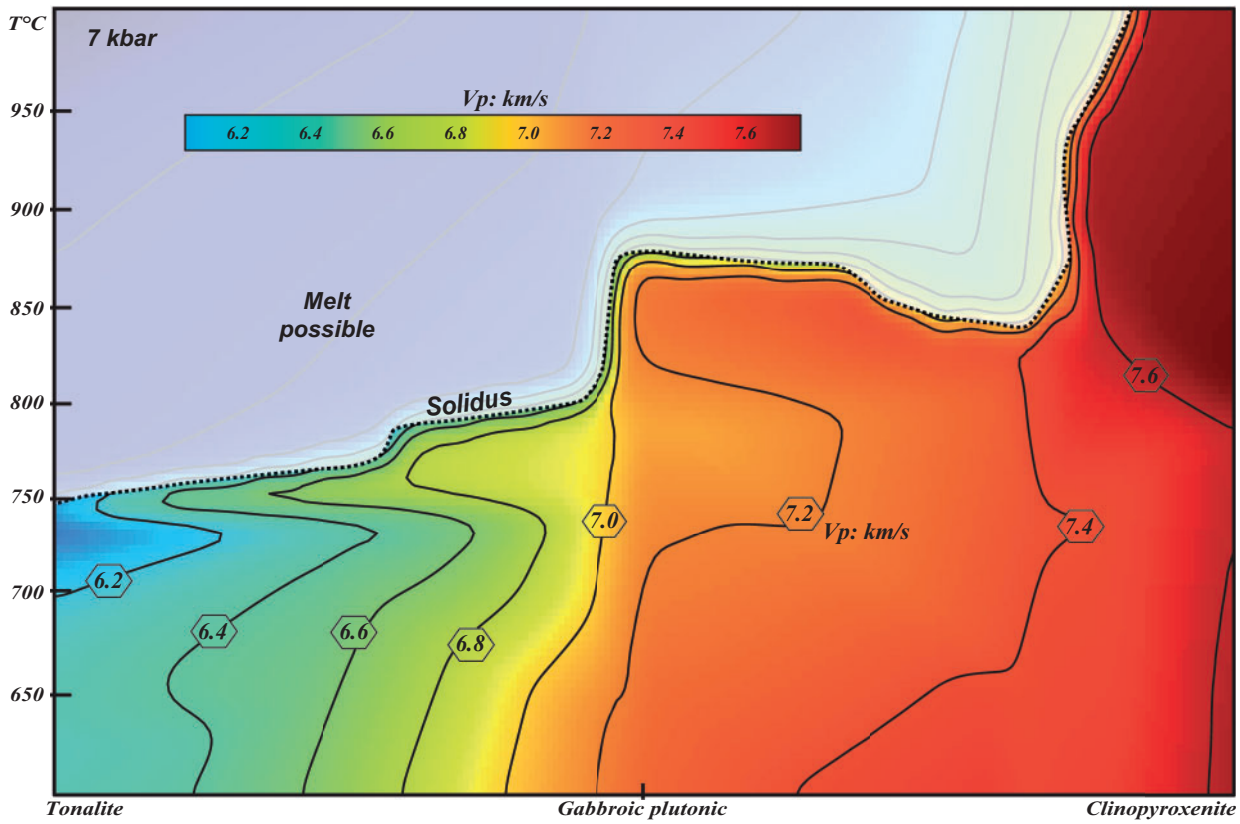

Fig. 16. Calculated seismic P-wave velocity as a function of temperature and composition at 7 kbar. The calculation uses mineral thermodynamic properties from Holland & Powell (1998) computed with Perple_X (Connolly, 2005, 2009). Calculation in the system NCFMASHT, with the clinopyroxenite being represented by Pipe 1 average clinopyroxenite, the gabbro being an average of the host metaplutonic rocks of Sapat (Bouilhol, 2008), and the tonalite being sample G32, a sill from the host layered rocks (Bouilhol, 2008). Bulk-rock major compositions used for the calculation are in Electronic Data Appendix 2. Solidus line is calculated with a melt model from Bouilhol *et al.* (2015), which is a modified version of that of White *et al.* (2001). The solidus is calculated from the bulk composition of the considered rocks, and is thus sensitive to the cumulative character of the rock [i.e. the bulk composition may approach pure cumulate (clinopyroxenite) to close to liquid composition (tonalite)].

CONCLUSIONS

The lower arc crust exposed in the Sapat Complex of the Kohistan paleo-island arc hosts ultramafic pipes that represent magmatic conduits in which melt rose, fractionated and partly reacted with its own cumulates during ascent from the mantle towards higher crustal levels. The crystallization sequence indicates that the cumulates formed during differentiation of mantle-derived basaltic magmas containing >5 wt % H_2O, with the early stages dominated by ol, spl and cpx, maintaining the composition of the transferred melts on the equivalent cotectic. Hornblende appears first at the expense of cpx, driving the melt to a basaltic–andesitic composition. Peritectic opx follows, before the appearance of An-rich plagioclase. Hornblende and especially An-rich plagioclase become important during the latest stages of melt differentiation when trapped melts fractionate *in situ* towards tonalitic compositions. This crystallization sequence illustrates the complex peritectic reactions taking place with decreasing temperature. Furthermore, fluid-precipitated minerals and evidence for re-equilibration indicate that the parental mantle melt reached water-saturation relatively early in its differentiation path, when hbl was present as a peritectic phase.

The observed structures suggest that the pipes intruded along brittle–ductile structures and grew through thermal and chemical erosion of their host-rocks. The concentric zoning is suggestive of the open central axes of the pipes providing hundreds of meters wide, easy pathways for rising melts whereas cumulates precipitated at the pipe walls. As such, the pipes of the Sapat Complex provide evidence for a 'plumbing system' capable of sustaining pathways for large melt fluxes. The size and characteristics of these pipes fit the high-velocity 'columns' identified in seismic images of active arcs.

ACKNOWLEDGEMENTS

J.-L. Bodinier (Montpellier) is thanked for discussion and his participation in the Sapat project. We sincerely thank E. Reusser (ETH), L. Zehnder (ETH) and O. Bruguier (Montpellier) for analytical support. H. Dawood and S. Hussain (Pakistan) are sincerely acknowledged for efficient support. We also acknowledge J. Blundy and J.P. Davidson for fruitful discussions. Anonymous reviewers are thanked for their comments and suggestions. The patience of Marjorie Wilson and Alastair Lumsden is highly appreciated.

FUNDING

This study has been made possible by ETH-grant number 0-20220-04 and finalized under ERC grant StG 279828.

SUPPLEMENTARY DATA

Supplementary data for this paper are available at *Journal of Petrology* online.

REFERENCES

Alonso-Perez, R., Muntener, O. & Ulmer, P. (2009). Igneous garnet and amphibole fractionation in the roots of island arcs: experimental constraints on andesitic liquids. *Contributions to Mineralogy and Petrology* **157**, 541–558.

Annen, C., Blundy, J. D. & Sparks, R. S. J. (2006). The genesis of intermediate and silicic magmas in deep crustal hot zones. *Journal of Petrology* **47**, 505–539.

Ballhaus, C. & Berry, R. F. (1991). Crystallization pressure and cooling history of the Giles layered igneous complex, Central Australia. *Journal of Petrology* **32**, 1–28.

Bard, J. P. (1983). Metamorphism of an obducted island-arc: Example of the Kohistan sequence (Pakistan) in the Himalayan collided range. *Earth and Planetary Science Letters* **65**, 133–144.

Bouilhol, P. (2008). *Structural, petrological and geochemical constraints on transfer and evolution of arc-magmas in the mafic–ultramafic Sapat complex (Kohistan; Northern Pakistan)*. Zurich: ERDW ETH, 179 pp.

Bouilhol, P., Burg, J. P., Bodinier, J. L., Schmidt, M. W., Dawood, H. & Hussain, S. (2009). Magma and fluid percolation in arc to fore-arc mantle: Evidence from Sapat (Kohistan, Northern Pakistan). *Lithos* **107**, 17–37.

Bouilhol, P., Connolly, J. A. D. & Burg, J.-P. (2011a). Geological evidence and modeling of melt migration by porosity waves in the sub-arc mantle of Kohistan (Pakistan). *Geology* **39**, 1091–1094.

Bouilhol, P., Schaltegger, U., Chiaradia, M., Ovtcharova, M., Stracke, A., Burg, J.-P. & Dawood, H. (2011b). Timing of juvenile arc crust formation and evolution in the Sapat Complex (Kohistan-Pakistan). *Chemical Geology* **280**, 243–256.

Bouilhol, P., Burg, J.-P., Bodinier, J.-L., Schmidt, M. W., Bernasconi, S. M. & Dawood, H. (2012). Gem olivine and calcite mineralization precipitated from subduction-derived fluids in the Kohistan arc-mantle (Pakistan). *Canadian Mineralogist* **50**, 1291–1304.

Bouilhol, P., Jagoutz, O., Hanchar, J. M. & Dudas, F. O. (2013). Dating the India–Eurasia collision through arc magmatic records. *Earth and Planetary Science Letters* **366**, 163–175.

Bouilhol, P., Magni, V., van Hunen, J. & Kaislaniemi, L. (2015). A numerical approach to melting in warm subduction zones. *Earth and Planetary Science Letters* **411**, 37–44.

Brophy, J. G. (2008). A study of rare earth element (REE)–SiO_2 variations in felsic liquids generated by fractionation and amphibolite melting: a potential test for discriminating the two different processes. *Contributions to Mineralogy and Petrology* **155**, 337–357.

Burg, J. P. (2011). The Asia–Kohistan–India collision. Review and discussion. In: Brown, D. & Ryan, P. D. (eds) *Arc–Continent Collision*. Springer, pp. 279–309.

Burg, J. P., Bodinier, J. L., Chaudhry, S., Hussain, S. & Dawood, H. (1998). Infra-arc mantle–crust transition and intra-arc mantle diapirs in the Kohistan Complex (Pakistani Himalaya): petro-structural evidence. *Terra Nova* **10**, 74–80.

Burg, J. P., Jagoutz, O., Dawood, H. & Hussain, S. S. (2006). Precollision tilt of crustal blocks in rifted island arcs: Structural evidence from the Kohistan Arc. *Tectonics* **25**, 1–13.

Cawthorn, R. G. (1976). Melting relations in part of system CaO–MgO–Al_2O_3–SiO_2–Na_2O–H_2O under 5 Kb pressure. *Journal of Petrology* **17**, 44–72.

Cawthorn, R. G. & O'Hara, M. J. (1976). Amphibole fractionation in calc-alkaline magma genesis. *American Journal of Science* **276**, 309–329.

Chamberlain, C. P., Zeitler, P. K. & Erickson, E. (1991). Constraints on the tectonic evolution of the northwestern Himalaya from geochronological and petrologic studies of Babusar Pass, Pakistan. *Journal of Geology* **99**, 829–849.

Claeson, D. T. (1998). Coronas, reaction rims, symplectites and emplacement depth of the Rymmen gabbro, Transscandinavian Igneous Belt, southern Sweden. *Mineralogical Magazine* **62**, 743–757.

Connolly, J. A. D. (2005). Computation of phase equilibria by linear programming: A tool for geodynamic modeling and its application to subduction zone decarbonation. *Earth and Planetary Science Letters* **236**, 524–541.

Connolly, J. A. D. (2009). The geodynamic equation of state: What and how. *Geochemistry, Geophysics, Geosystems* **10**, Q10014.

Cruciani, G., Franceschelli, M., Groppo, C., Brogioni, N. & Vaselli, O. (2008). Formation of clinopyroxene plus spinel and amphibole plus spinel symplectites in coronitic gabbros from the Sierra de San Luis (Argentina): a key to post-magmatic evolution. *Journal of Metamorphic Geology* **26**, 759–774.

Davidson, J., Turner, S., Handley, H., Macpherson, C. & Dosseto, A. (2007). Amphibole 'sponge' in arc crust? *Geology* **35**, 787–790.

DeBari, S. M. & Coleman, R. G. (1989). Examination of the deep levels of an island-arc—Evidence from the Tonsina ultramafic–mafic assemblage, Tonsina, Alaska. *Journal of Geophysical Research* **94**, 4373–4391.

DeBari, S. M. & Sleep, N. H. (1991). High-Mg, low-Al bulk composition of the Talkeetna island-arc, Alaska—implications for primary magmas and the nature of arc crust. *Geological Society of America Bulletin* **103**, 37–47.

de Haas, G., Nijland, T. G., Valbracht, P. J., Maijer, C., Verschure, R. & Andersen, T. (2002). Magmatic versus metamorphic origin of olivine–plagioclase coronas. *Contributions to Mineralogy and Petrology* **143**, 537–550.

Dhuime, B., Bosch, D., Bodinier, J. L., Garrido, C. J., Bruguier, O., Hussain, S. S. & Dawood, H. (2007). Multistage evolution of the Jijal ultramafic–mafic complex (Kohistan, N Pakistan): Implications for building the roots of island arcs. *Earth and Planetary Science Letters* **261**, 179–200.

Ehlers, E. G. (1972). *The Interpretation of Geological Phase Diagrams*. Dover.

Feig, S. T., Koepke, J. & Snow, J. E. (2006). Effect of water on tholeiitic basalt phase equilibria: an experimental study under oxidizing conditions. *Contributions to Mineralogy and Petrology* **152**, 611–638.

Foden, J. D. & Green, D. H. (1992). Possible role of amphibole in the origin of andesite—some experimental and natural evidence. *Contributions to Mineralogy and Petrology* **109**, 479–493.

Frei, D., Liebscher, A., Franz, G. & Dulski, P. (2004). Trace element geochemistry of epidote minerals. In: Liebscher, A. & Franz, G. (eds) *Epidotes. Mineralogical Society of America and Geochemical Society, Reviews in Mineralogy and Geochemistry* **56**, 553–605.

Garrido, C. J., Bodinier, J. L., Burg, J. P., Zeilinger, G., Hussain, S. S., Dawood, H., Chaudhry, M. N. & Gervilla, F. (2006). Petrogenesis of mafic garnet granulite in the lower crust of the Kohistan paleo-arc complex (Northern

Pakistan): Implications for intra-crustal differentiation of island arcs and generation of continental crust. *Journal of Petrology* **47**, 1873–1914.

Garrido, C. J., Bodinier, J. L., Dhuime, B., Bosch, D., Chanefo, I., Bruguier, O., Hussain, S. S., Dawood, H. & Burg, J. P. (2007). Origin of the island arc Moho transition zone via melt–rock reaction and its implications for intracrustal differentiation of island arcs: Evidence from the Jijal complex (Kohistan complex, northern Pakistan). *Geology* **35**, 683–686.

Gillis, K. M. & Meyer, P. S. (2001). Metasomatism of oceanic gabbros by late stage melts and hydrothermal fluids: Evidence from the rare earth element composition of amphiboles. *Geochemistry, Geophysics, Geosystems* **2**, paper number: 2000gc000087.

Green, T. & Ringwood, A. E. (1968). Genesis of the calc-alkaline igneous rock suite. *Contributions to Mineralogy and Petrology* **18**, 105–162.

Greene, A. R., DeBari, S. M., Kelemen, P. B., Blusztajn, J. & Clift, P. D. (2006). A detailed geochemical study of island arc crust: the Talkeetna Arc section, south–central Alaska. *Journal of Petrology* **47**, 1051–1093.

Grove, T. L., Donnelly-Nolan, J. M. & Housh, T. (1997). Magmatic processes that generated the rhyolite of Glass Mountain, Medicine Lake volcano, N. California. *Contributions to Mineralogy and Petrology* **127**, 205–223.

Grove, T. L., Elkins-Tanton, L. T., Parman, S. W., Chatterjee, N., Muntener, O. & Gaetani, G. A. (2003). Fractional crystallization and mantle-melting controls on calc-alkaline differentiation trends. *Contributions to Mineralogy and Petrology* **145**, 515–533.

Grove, T. L., Chatterjee, N., Parman, S. W. & Medard, E. (2006). The influence of H_2O on mantle wedge melting. *Earth and Planetary Science Letters* **249**, 74–89.

Gunther, D. & Heinrich, C. A. (1999). Enhanced sensitivity in laser ablation-ICP mass spectrometry using helium–argon mixtures as aerosol carrier—Plenary lecture. *Journal of Analytical Atomic Spectrometry* **14**, 1363–1368.

Helmy, H. M., Yoshikawa, M., Shibata, T., Arai, S. & Tamura, A. (2008). Corona structure from arc mafic–ultramafic cumulates: The role and chemical characteristics of late-magmatic hydrous liquids. *Journal of Mineralogical and Petrological Sciences* **103**, 333–344.

Holland, T. J. B. & Powell, R. (1998). An internally consistent thermodynamic data set for phases of petrological interest. *Journal of Metamorphic Geology* **16**, 309–343.

Ikeda, T., Nishiyama, T., Yamada, S. & Yanagi, T. (2007). Microstructures of olivine–plagioclase corona in meta-ultramafic rocks from Sefuri Mountains, NW Kyushu, Japan. *Lithos* **97**, 289–306.

Jackson, M. D., Gallagher, K., Petford, N. & Cheadle, M. J. (2005). Towards a coupled physical and chemical model for tonalite–trondhjemite–granodiorite magma formation. *Lithos* **79**, 43–60.

Jagoutz, O. E. (2010). Construction of the granitoid crust of an island arc. Part II: a quantitative petrogenetic model. *Contributions to Mineralogy and Petrology* **160**, 359–381.

Jagoutz, O. & Schmidt, M. W. (2012). The formation and bulk composition of modern juvenile continental crust: The Kohistan arc. *Chemical Geology* **298–299**, 79–96.

Jagoutz, O., Muntener, O., Burg, J. P., Ulmer, P. & Jagoutz, E. (2006). Lower continental crust formation through focused flow in km-scale melt conduits: The zoned ultramafic bodies of the Chilas complex in the Kohistan island arc (NW Pakistan). *Earth and Planetary Science Letters* **242**, 320–342.

Jagoutz, O., Müntener, O., Schmidt, M. W. & Burg, J.-P. (2011). The roles of flux- and decompression melting and their respective fractionation lines for continental crust formation: Evidence from the Kohistan arc. *Earth and Planetary Science Letters* **303**, 25–36.

Jan, M. Q. & Howie, R. A. (1981). The mineralogy and geochemistry of the metamorphosed basic and ultrabasic rocks of the Jijal Complex, Kohistan, NW Pakistan. *Journal of Petrology* **22**, 85–126.

Jan, M. Q. & Windley, B. F. (1990). Chromian spinel silicate chemistry in ultramafic rocks of the Jijal Complex, Northwest Pakistan. *Journal of Petrology* **31**, 667–715.

Kaegi, R. (2000). *The liquid line of descent of hydrous, primary, calc-alkaline magmas under elevated pressure. An experimental approach*. ETH, 163 pp.

Kelemen, P. B., Hirth, G., Shimizu, N., Spiegelman, M. & Dick, H. J. B. (1997). A review of melt migration processes in the adiabatically upwelling mantle beneath oceanic spreading ridges. *Philosophical Transactions of the Royal Society of London, Series A* **355**, 283–318.

Kodaira, S., Sato, T., Takahashi, N., Ito, A., Tamura, Y., Tatsumi, Y. & Kaneda, Y. (2007). Seismological evidence for variable growth of crust along the Izu intraoceanic arc. *Journal of Geophysical Research: Solid Earth* **112**, doi:10.1029/2006JB004593.

Krawczynski, M. J., Grove, T. L. & Behrens, H. (2012). Amphibole stability in primitive arc magmas: effects of temperature, H_2O content, and oxygen fugacity. *Contributions to Mineralogy and Petrology* **164**, 317–339.

Martel, C., Pichavant, M., Holtz, F., Scaillet, B., Bourdier, J. L. & Traineau, H. (1999). Effects of $f(O_2)$ and H_2O on andesite phase relations between 2 and 4 kbar. *Journal of Geophysical Research: Solid Earth* **104**, 29453–29470.

Melekhova, E., Blundy, J., Robertson, R. & Humphreys, M. (2015). Experimental evidence for polybaric differentiation of primitive arc basalt beneath St. Vincent, Lesser Antilles. *Journal of Petrology* **56**, 161–192.

Muntener, O. & Ulmer, P. (2006). Experimentally derived high-pressure cumulates from hydrous arc magmas and consequences for the seismic velocity structure of lower arc crust. *Geophysical Research Letters* **33**, 5.

Muntener, O., Kelemen, P. B. & Grove, T. L. (2001). The role of H_2O during crystallization of primitive arc magmas under uppermost mantle conditions and genesis of igneous pyroxenites: an experimental study. *Contributions to Mineralogy and Petrology* **141**, 643–658.

Murray, C. G. (1972). Zoned ultramafic complexes of the Alaskan type: feeder pipes of andesitic volcanoes. *Geological Society of America*, Memoir 132, 313–335.

Nandedkar, R., Ulmer, P. & Müntener, O. (2014). Fractional crystallization of primitive, hydrous arc magmas: an experimental study at 0·7 GPa. *Contributions to Mineralogy and Petrology* **167**, 1–27.

Nicolas, A., Boudier, F., Koepke, J., France, L., Ildefonse, B. & Mevel, C. (2008). Root zone of the sheeted dike complex in the Oman ophiolite. *Geochemistry, Geophysics, Geosystems* **9**, 29, doi:10.1029/2007GC001918.

Pearce, N. J. G., Perkins, W. T., Westgate, J. A., Gorton, M. P., Jackson, S. E., Neal, C. R. & Chenery, S. P. (1997). A compilation of new and published major and trace element data for NIST SRM 610 and NIST SRM 612 glass reference materials. *Geostandards Newsletter* **21**, 115–144.

Petford, N. & Gallagher, K. (2001). Partial melting of mafic (amphibolitic) lower crust by periodic influx of basaltic magma. *Earth and Planetary Science Letters* **193**, 483–499.

Pichavant, M. & Macdonald, R. (2007). Crystallization of primitive basaltic magmas at crustal pressures and genesis of the calc-alkaline igneous suite: experimental evidence from St

Vincent, Lesser Antilles arc. *Contributions to Mineralogy and Petrology* **154**, 535–558.

Pichavant, M., Martel, C., Bourdier, J. L. & Scaillet, B. (2002a). Physical conditions, structure, and dynamics of a zoned magma chamber: Mount Pelee (Martinique, Lesser Antilles Arc). *Journal of Geophysical Research: Solid Earth* **107**, 29, doi: 10.1029/2001JB000315.

Pichavant, M., Mysen, B. O. & Macdonald, R. (2002b). Source and H_2O content of high-MgO magmas in island arc settings: An experimental study of a primitive calc-alkaline basalt from St. Vincent, Lesser Antilles arc. *Geochimica et Cosmochimica Acta* **66**, 2193–2209.

Prouteau, G. & Scaillet, B. (2003). Experimental constraints on the origin of the 1991 Pinatubo dacite. *Journal of Petrology* **44**, 2203–2241.

Ringuette, L., Martignole, J. & Windley, B. F. (1999). Magmatic crystallization, isobaric cooling, and decompression of the garnet-bearing assemblages of the Jijal sequence (Kohistan terrane, western Himalayas). *Geology* **27**, 139–142.

Rodriguez, C., Selles, D., Dungan, M., Langmuir, C. & Leeman, W. (2007). Adakitic dacites formed by intracrustal crystal fractionation of water-rich parent magmas at Nevado de Longaví volcano (36·2°S; Andean Southern Volcanic Zone, central Chile). *Journal of Petrology* **48**, 2033–2061.

Romick, J. D., Kay, S. M. & Kay, R. W. (1992). The influence of amphibole fractionation on the evolution of calc-alkaline andesite and dacite tephra from the central Aleutians, Alaska. *Contributions to Mineralogy and Petrology* **112**, 101–118.

Schaltegger, U., Zeilinger, G., Frank, M. & Burg, J. P. (2002). Multiple mantle sources during island arc magmatism: U–Pb and Hf isotopic evidence from the Kohistan arc complex, Pakistan. *Terra Nova* **14**, 461–468.

Schmidt, M. W. (1992). Amphibole composition in tonalite as a function of pressure—an experimental calibration of the Al-in-hornblende thermometer. *Contributions to Mineralogy and Petrology* **110**, 304–310.

Schmidt, M. W. & Thompson, A. B. (1996). Epidote in calc-alkaline magmas: An experimental study of stability, phase relationships, and the role of epidote in magmatic evolution. *American Mineralogist* **81**, 462–474.

Shillington, D. J., Van Avendonk, H. J. A., Holbrook, W. S., Kelemen, P. B. & Hornbach, M. J. (2004). Composition and structure of the central Aleutian island arc from arc-parallel wide-angle seismic data. *Geochemistry, Geophysics, Geosystems* **5**, 32, doi:10.1029/2004GC000715.

Sisson, T. W. & Grove, T. L. (1993). Experimental investigations of the role of H_2O in calc-alkaline differentiation and subduction zone magmatism. *Contributions to Mineralogy and Petrology* **113**, 143–166.

Smith, D. R. & Leeman, W. P. (1987). Petrogenesis of Mount St Helens dacitic magmas. *Journal of Geophysical Research: Solid Earth and Planets* **92**, 10313–10334.

Sun, S.-S. & McDonough, W. F. (1989). Chemical and isotopic systematics of oceanic basalts: implications for mantle composition and processes. In: Saunders, A. D. & Norry, M. J. (eds) *Magmatism in the Ocean Basins. Geological Society, London, Special Publications* **42**, 313–345.

Tahirkheli, R. A. (1979). Geology of Kohistan and adjoining Eurasian and Indo-Pakistan continents, Pakistan. *Geological Bulletin, University of Peshawar* **11**, 1–30.

Takahashi, N., Kodaira, S., Tatsumi, Y., Kaneda, Y. & Suyehiro, K. (2008). Structure and growth of the Izu–Bonin–Mariana arc crust: 1. Seismic constraint on crust and mantle structure of the Mariana arc–back-arc system. *Journal of Geophysical Research: Solid Earth* **113**, 18, doi:10.1029/2007JB005120.

Tatsumi, Y., Sakuyama, M., Fukuyama, H. & Kushiro, I. (1983). Generation of arc basalt magmas and thermal structure of the mantle wedge in subduction zones. *Journal of Geophysical Research* **88**, 5815–5825.

Treloar, P. J., Petterson, M. G., Jan, M. Q. & Sullivan, M. A. (1996). A re-evaluation of the stratigraphy and evolution of the Kohistan arc sequence, Pakistan Himalaya: Implications for magmatic and tectonic arc-building processes. *Journal of the Geological Society, London* **153**, 681–693.

Ulmer, P. (2001). Partial melting in the mantle wedge—the role of H_2O in the genesis of mantle-derived 'arc-related' magmas. *Physics of the Earth and Planetary Interiors* **127**, 215–232.

Ulmer, P. (2007). Differentiation of mantle-derived calc-alkaline magmas at mid to lower crustal levels: experimental and petrologic constraints. *Periodico di Mineralogia* **76**, 309–325.

van Achterbergh, E., Ryan, C. G., Jackson, S. E. & Griffin, W. L. (2001). Data reduction software for LA-ICP-MS. In: Sylvester, P. (ed.) *Laser Ablation ICP-MS in the Earth Sciences: Current Practices and Outstanding Issues. Mineralogical Association of Canada, Short Course Series* **40**, 239–243.

White, R. W., Powell, R. & Holland, T. J. B. (2001). Calculation of partial melting equilibria in the system Na_2O–CaO–K_2O–FeO–MgO–Al_2O_3–SiO_2–H_2O (NCKFMASH). *Journal of Metamorphic Geology* **19**, 139–153.

Wood, B. J. & Blundy, J. D. (1997). A predictive model for rare earth element partitioning between clinopyroxene and anhydrous silicate melt. *Contributions to Mineralogy and Petrology* **129**, 166–181.

Yamamoto, H. & Yoshino, T. (1998). Superposition of replacements in the mafic granulites of the Jijal complex of the Kohistan arc, northern Pakistan: dehydration and rehydration within deep arc crust. *Lithos* **43**, 219–234.

Zeilinger, G. (2002). *Structural and geochronological study of the Lowest Kohistan Complex, Indus Kohistan region in Pakistan, NW Himalaya*. ETH, 243 pp.

Zen, E. A. & Hammarstrom, J. M. (1984). Magmatic epidote and its petrologic significance. *Geology* **12**, 515–518.